Ion Energy Balance in Pulsator

F. Wagner

IPP III/52 October 1979

MAX-PLANCK-INSTITUT FÜR PLASMAPHYSIK

8046 GARCHING BEI MÜNCHEN

MAX-PLANCK-INSTITUT FÜR PLASMAPHYSIK

GARCHING BEI MÜNCHEN

Ion Energy Balance in Pulsator

F. Wagner

IPP III/52 October 1979

Die nachstehende Arbeit wurde im Rahmen des Vertrages zwischen dem Max-Planck-Institut für Plasmaphysik und der Europäischen Atomgemeinschaft über die Zusammenarbeit auf dem Gebiete der Plasmaphysik durchgeführt.

IPP III/ 52 F. Wagner Ion Energy Balance in Pulsator

Abstract

Radial profiles of the ion temperature and neutral-gas density were measured on Pulsator during high density discharges. The ion energy balance shows good agreement with the neoclassical heat conductivity coefficient of Galeev and Sagdeev. Cases with anomalous ion heat transport are observed predominantly at high plasma current and low plasma densities. Radial profiles of the energy confinement times for ions and electrons are determined. They show that there is a gradual transition from electron-dominated energy transport to ion-dominated energy transport with increasing density. At high density, the limiting influence of internal disruption on the electron energy confinement time is observed.

I. Introduction

The ions in an ohmically heated tokamak plasma gain energy in the plasma interior by collisions with the electrons and lose energy by heat conduction, particle diffusion and charge exchange. The common conclusion from the ion energy balance, investigated in several tokmakak plasmas /1-4/ is that the ions follow neoclassical scaling laws. For TFR, however, the neoclassical heat conductivity coefficient had to be increased by a factor of up to 10 to reproduce the ion temperature values measured in hydrogen discharges /5/.

In this report, we investigate the ion energy balance for ohmically heated hydrogen discharges in the Pulsator tokamak. The principal difference in the ion energy balance of a Pulsator plasma compared with previous investigations is a low neutral-gas density in the plasma centre as a consequence of a high electron density achieved by gas puffing. The ion energy balance is studied in the peak electron density range from $1.8 \times 10^{13} cm^{-3}$ to $1.9 \times 10^{14} cm^{-3}$. The corresponding neutral-gas density in the plasma centre ranges from $1.4 \times 10^{9} cm^{-3}$ to $4 \times 10^{7} cm^{-3}$. Consequently, the charge exchange and particle diffusion terms are reduced to negligible loss terms in the plasma centre at increased density.

Another consequence of the high plasma density is an increase of the power transferred from the electrons to the ions with the result that the ion temperature T_i approaches the electron temperature T_e. Therefore, the ion energy balance has to be studied with $T_e - T_i \ll T_e$.

The purpose of this report is to investigate the ion energy balance in Pulsator for 5 distinct types of discharges.

1. Discharge with impurity accumulation

One type of Pulsator discharge shows the phenomenon of impurity accumulation (IA). During the last 10 ms of the discharge prior to disruption the signals of those Si surface diodes viewing the plasma centre show that the internal disruptions stop and indicate an increase in X-ray radiation. These phenomena are attributed to impurity accumulation in the plasma centre caused by inwardly directed neoclassical transport no longer counteracted by internal disruption /6/.

The ion energy balance of two discharges of this type are analyzed here: One discharge is terminated at a line average density $\bar{n}_e$ of $8.7 \times 10^{13} cm^{-3}$ the other is terminated at $\bar{n}_e = 6.2 \times 10^{13} cm^{-3}$ by disruption. The plasma current $I_p = 55$ kA and safety factor $q(a) = 4.2$ are the same for both discharges. In the following this type of discharge is referred to by the abbreviation: Discharge IA-8.7 and IA-6.2, respectively.

2. Discharge with density limit

Another type of Pulsator discharge can be characterized by the observation of a density limit at an average density of $1.12 \times 10^{14} cm^{-3}$ /7/. Plasma current ($I_p = 55$ kA) and safety-factor ($q(a) = 4.2$) are the same as in discharge IA-8.7. The increase in density in this type of discharge (referred to as discharge DL) is somewhat higher than in discharge IA-8.7 (see Fig.1). This causes a difference in the prevailing transport characteristics since in discharge DL internal disruption is observed till the plasma disrupts and no impurity accumulation occurs.

3. Discharge at high plasma current

The third type of discharge is characterized by a high plasma current of 88 kA. As the toroidal magnetic field B_T is kept

constant at 27.5 kG, q(a) is reduced to 2.7. In this type of discharge a high line density of $1.32 \times 10^{14} cm^{-3}$ is achieved (in the last 55 ms of the discharge by utilizing the helical windings of Pulsator). In this type of discharge saw-tooth is active with $\frac{\Delta T_e}{T_e} \simeq 15$ % till plasma disruption. This type of discharge is referred to as discharge HC.

4. Discharge at low plasma current

The plasma current of this discharge is 40 kA. q(a) is kept at 4.3 by reducing the toroidal magnetic field to 20 kG. The average density achieved before the plasma disrupts is $6.5 \times 10^{13} cm^{-3}$. This type of discharge is referred to as discharge LC.

5. Discharge at low density

For comparison the 4 high density discharges are supplemented by a low-density discharge at an average density of $1.2 \times 10^{13} cm^{-3}$. This discharge is abbreviated as discharge LD.

The major characteristics of the 5 types of discharges analyzed here are summarized in Table I. The time dependence of the average density of the different discharges 1 - 4 are measured by the central channel of a 2 mm μ-wave system and is plotted in Fig.1. The different rates of density increase are achieved by differently programming the pulsed gas valve.

II. Measurement of the ion temperature and neutral-gas density

The ion temperature is measured by the passive charge exchange technique applying a 5-channel neutral particle analyzer /8/. The analyzer can be moved in a poloidal plane so that radial flux and temperature profiles from r = + 11 cm to r = - 9 cm can be measured. The limiter radius is 11 cm.

The charge exchange flux spectra $d\Phi/dE$ show an exponential tail in the energy range from 3 $T_i(0)$ to (8-10)$T_i(0)$, indicating a Maxwellian ion population. The ion temperature is deduced from the slope of the energy spectrum of the neutral density $4\pi/v d\Phi/dE$ in this energy range (v = particle velocity). One has to bear in mind, however, that the exponential tail of the spectrum is composed of flux contributions of different plasma zones with different ion temperatures. The consequence at high densities is that the ion temperature determined in this way is underestimated and has to be corrected.

The neutral-gas density $n_o(r)$ is determined from the AURORA computer program, which applies a Monte Carlo technique /9/. Input parameters to this code are experimental values of the electron density $n_e(r)$, $T_e(r)$ and $T_i(r)$. The ion density $n_i(r)$ is determined from the measured Z_{eff} value by assuming O^{8+} as the only impurity. Z_{eff} is assumed to be constant across the plasma cross-section. As Z_{eff} is between 1.5 and 2, no great error is introduced by the ion depletion factor. The energy of the cold neutrals penetrating the plasma is set at 3 eV.

With the neutral-gas density calculated from the Monte Carlo code the flux spectrum of emitted particles can be determined:

$$d\phi/dE = \frac{1}{2\pi^{3/2}} \int_{-a}^{a} n_i(r) n_o(r) \; X_{cx}(r) e^{-\frac{E}{T_i}} \frac{E^{1/2}}{T_i^{3/2}} e^{-\int_r^a \frac{dr'}{\lambda}} dr \quad (1)$$

X_{cx} = charge exchange rate coefficient determined by averaging over the neutral distribution, which is set equal to the ion distribution for this purpose.

λ = mean free path of charge exchange neutrals.

The calculated flux spectra can be compared with the experimental flux spectra which are obtained absolutely by the calibrated neutral particle analyzer. The calibration for particle fluxes is accurate to 30 %.

The comparison between experimental data with the calculated spectrum yields:

1. from the slope of the spectrum
   at high density a correction to the experimental T_i values deduced from the tail of the density spectrum in the energy range $E > 3\ T_i(0)$. At high density T_i data taken from passive charge exchange are underestimated owing to profile effects along the line of sight and to particle reabsorption. The correction to the experimental T_i data in the plasma centre increases with the electron density. At the highest central density of $1.9 \times 10^{14} cm^{-3}$ the experimental $T_i(0)$ deduced from the slope of the energy spectrum of the neutrals has to be increased by 16 % to correct for the above mentioned effects.
2. from the absolute value of the spectrum
   the neutral edge density. Without knowledge of the neutral edge density, the neutral density profile can only be determined relatively from the Monte Carlo code. By appropriate choice of the neutral edge density in the Monte Carlo program the calculated flux spectrum from

eq. (1) can be fitted to the experimental points in the range $E \geq 3\ T_i(0)$. By this procedure, the neutral edge density is found and with this input value into the Monte Carlo code the neutral-gas density profile is determined absolutely.

Figure 2 shows two examples of flux spectra emitted from the plasma centre. Curve 1 is obtained at a low central density of $1.8 \times 10^{13} cm^{-3}$. With the gas input, the emitted particle flux is increased for all energies. As can be readily seen from the exponential tail of the spectra, this enhancement increases with energy, indicating an increase in the central ion temperature caused by improved coupling between electrons and ions.

The neutral gas densities for the two cases are shown as insert to Fig.2. Owing to the gas input the neutral edge density is increased but owing to the high electron density the neutral gas density in the plasma centre is decreased by nearly two orders of magnitude.

The solid lines through the flux data points are obtained from eq.1 with the neutral gas density profiles determined from the Monte Carlo code and shown as insert to Fig.2.

For all cases for which the ion energy balance is studied and which are discussed below, the neutral gas density has been determined. In Fig.3a central values of the neutral gas density and in Fig.3b the ratio of the central density $n_o(0)$ to the edge neutral density $n_o(a)$ are plotted versus the average electron density, indicating the depletion of the neutral gas in the plasma centre with increased electron density.

III. Evolution of the ion temperature during high-density Pulsator discharges.

Figures 4a and b show the time dependence of the central ion temperature for six different cases.

- For comparison with high-density discharges, $T_i(t)$ of a discharge without additional gas input (LD) is shown in Fig.4a. T_i stays roughly constant between 100 eV and 120 eV. The average electron density in this case is $1 \times 10^{13} cm^{-3}$.

- The other five cases shown in Fig.4a and in Fig.4b give the time dependence of T_i of the different types of discharge summarized in Table I.

Figures 4a and b demonstrate first of all the effect of density build-up on the ion temperature. T_i rises from about 100 eV, the typical value at low density, to values beyond 450 eV. In all cases, gas puffing is started at 15 ms after breakdown. The increase in T_i is most rapid for case HC and case LC and slowest for case IA-6.2. This behaviour agrees well with the different slopes with which the density increases (see Fig.1).

A comparison of the T_i values of the different discharges before 15 ms (when the density is the same for all five cases) shows that T_i is highest for case HC and lowest for case LC. At 15 ms the plasma current of discharge HC is 70 kA compared with the 40 kA of discharge LC. The plasma current in the other four cases is 55 kA. Qualitatively, the dependence of T_i on the plasma density and current shown in Figs.4a and b agrees with neoclassical expectations /4/.

The time dependence of discharges DL and IA-8.7 are separately shown in Fig.4b. Both discharges have the same plasma current, and toroidal magnetic field, but differ somewhat in the temporal increase of density, giving rise to the above-mentioned impurity accumulation during the final 10 ms of discharge IA-8.7.

However, differences in both discharge types show up much earlier during the discharge in the variation of T_i with time. As can be seen in Fig.4b, T_i in case DL levels out at 50 ms at a value of 350 eV, while in case IA-8.7 it continues to rise to 450 eV though the density in this case is even less.

Differences in both discharges also show up in the time variation of the atomic flux emitted from the plasma exemplified in Fig.5 for particles at 1500 eV. There is an obvious increase in flux with the gas input.It is noteworthy, that the flux in case DL drops after a maximum is obtained at 60 ms contrary to case IA-8.7, where the flux stays roughly constant.

IV. Ion energy balance

The ion energy balance can be written

$$\frac{\partial E_i(r)}{\partial t} = P_{ei}(r) + P_{iz}(r) - P_{cx}(r) - P_D(r) - P_{hc}(r). \qquad (2)$$

First, we discuss the different terms of eq.(2). The units used are watt, eV, cm,s.

P_{ei} = power transferred from the electrons to the ions. The power density Q_{ei} transferred from the electrons to the ions is given by

$$Q_{ei}(r) = 1.25 \times 10^{-26} n_e^2(r) [Z] (T_e(r) - T_i(r)) T_e^{-3/2}$$

The total power within a volume of radius r is

$$P_{ei}(r) = 4\pi^2 R \int_0^r Q_{ei}(r') r' dr'$$

R = major radius (= 70 cm)

[Z] is calculated on the assumption that O^{8+} is the only impurity in Pulsator (for details see Ref. /1/).

P_{cx} = power lost by charge exchange

$$P_{cx}(r)=9.5 \times 10^{-18} R \int_0^r n_i(r') n_o(r') X_{cx}(r') (T_i(r')-T_o(r')) r' dr'$$

The determination of the neutral gas density $n_o(r)$ is described in Sec. II. $X_{cx}(r)$ is the rate coefficient for charge exchange. The temperature of the atoms T_o at radius r is set equal to the temperature of the ions at radius r': $r' = r + \lambda / \Gamma 3$.
At high densities the contribution of charge exchange to the ion energy balance in the plasma centre is reduced owing to the decrease of n_o but also because T_o comes close to T_i.

P_D = power lost by particle diffusion.
The power density transported by ion diffusion is

$$Q_D(r) = -\frac{3}{2} \frac{1}{r} \frac{\partial}{\partial r} \left(r D T_i \frac{\partial n_i}{\partial r}\right)$$

As proposed by /3/, the unknown diffusion coefficient is determined with the help of the particle continuity equation for a stationary plasma.

$$-\frac{1}{r} \frac{\partial}{\partial r} \left(r D \frac{\partial n_i}{\partial r}\right) = n_e(r) n_o(r) X_{ei}(r).$$

$X_{ei}(r)$ is the rate coefficient for electron impact ionization.
The total power lost by particle diffusion is then given by

$$P_D(r)=9.5 \times 10^{-18} R \frac{\partial}{\partial r} \left(T_i(r) \int_0^r n_o(r') n_e(r') X_{ei}(r') r' dr'\right)$$

The density rise in the plasma centre as achieved by gas puffing cannot in all cases be explained by ionization of the neutrals present in the plasma centre. As the occurrence of inverted density profiles is generally not observed, neoclassical transport towards the plasma centre /15/ has been claimed for Alcator. The effect of the density build-up in the plasma centre on the ion energy balance is discussed in more detail in Sec.IV.7.

P_{hc} = power lost by ion heat conduction.

$$P_{hc}(r) = -6.3 \times 10^{-18} R r n_i(r) X_i(r) \frac{\partial T_i}{\partial r}$$

Two cases are considered for the heat conductivity:
1. X_i as obtained by Hazeltine and Hinton /10/:

$$X_i=1.1 \times 10^{-2} q^2 n_e Z_{eff} B_{tor}^{-2} T_i^{-1/2} \frac{0.665(1+0.43\nu)}{\varepsilon^{3/2}+1.03\varepsilon^{3/4}\nu^{1/2}+0.185\nu} \quad (3)$$

$\varepsilon = r/R$; ν is the scattering parameter:

$$\nu = 7.7 \times 10^{-13} R n_e Z_{eff} q T_i^{-2} \quad (4)$$

Following Stott /1/, the enhancement factor Z_{ion} for the ion collision frequency due to impurity collisions has been approximated by $\sqrt{2}\, Z_{eff}$. The safety factor q(r) is calculated on the assumption that the current density is $j(r) \propto T_e(r)^{3/2}$.

2. χ_i as obtained by Galeev and Sagdeev /11/

$$\chi_i = 3.8 \times 10^{+10} T_i^{3/2} q\, B_{tor}^{-2}\, R^{-1} \qquad (5)$$

P_{iz} = power gained by electron impact ionization of charge exchange neutrals.

$$P_{iz}(r) = 9.5 \times 10^{-18} \int_o^r n_e(r') n_o(r') X_{ei}(r') T_o(r') r' dr'$$

$\frac{\partial E_i}{\partial t}$ = the power stored by the plasma ions.

$$\partial E_i(r)/\partial t = 9.5 \times 10^{-18} R \int_o^r (n_i(r') \frac{\partial T_i}{\partial t} + T_i(r') \frac{\partial n_i}{\partial t}) r' dr'$$

As the rate with which the density is increased in Pulsator is typically $1\text{-}2 \times 10^{15} cm^{-3} s^{-1}$, this term of the ion power balance cannot be neglected.

Equation (2) is solved numerically with the boundary conditions $\frac{\partial T_i(0)}{\partial r} = (0)$ and $T_i(a) = 20$ eV. The solution gives the ion temperature profile and the radial dependence of the different terms of the energy balance equation. A comparison of the calculated ion temperature profile with the measured profile allows evaluation of neoclassical heat conduction especially in the high-density cases where heat conduction represents the dominant ion loss.

Figures 6a to 24a show the different power contributions to the ion power balance (eq.(2)) versus radius for different moments during the discharges of Table I. For comparison, the ohmic heating power is plotted, too. The different power contributions are determined from the calculated T_i profile as obtained by solving eq.(2). The heat conductivity term is calculated from the coefficient of Hazeltine and Hinton (eq.(3)). The coefficient is multiplied, however, by a factor α so that the central values of T_i agree with the measured ones. The ion energy equation is balanced for all radii.

Part b of Figs.6 to 24 show the scattering parameter ν for ions calculated from eq. (4) by using the T_i profile as determined by solving the ion energy balance equation(solid line) or by using the experimental T_i data (dashed line). In both cases χ_i of Hazeltine and Hinton has been enhanced to match the central value of T_i. The difference between the curves reflect the uncertainty in the Ti profile as discussed in Sec.IV.10. Plotted into insert b are also the boundaries from the plateau regime to collisional or collisionless regimes.

Insert c gives the measured values of $T_i(r)$, if necessary corrected because of profile effects and attenuation. The solid lines on the left side of the ordinate are calculated T_i profiles based on the heat conductivity coefficient of Hazeltine and Hinton (eq.(3)) enhanced by a factor α which is given at the curve. The dashed curve on the right side of the ordinate is the T_i profile calculated using the heat conductivity coefficient of Galeev and Sagdeev (eq.(5)), again multiplied by a factor shown at the curve.

Measurements of the radial variation of the heat conductivity coefficient indicate that the assumption of a constant enhancement factor α is justified. This will be discussed in more detail in Sec.IV.8.

IV.1 Power balance for case IA-8.7

A comparison of the calculated T_i profiles with the measured profiles in Figs. 6 to 8 shows that the heat conductivity coefficient of Hazeltine and Hinton has to be moderately increased by a factor of about two to explain the central T_i data. This enhancement is within the accuracy with which the coefficient can be determined owing to imprecise knowledge of Z_{eff} and q(r). In the case of Galeev and Sagdeev the unmodified coefficient explains the measured T_i data. To summarize, in this type of discharge the neoclassical transport coefficient accounts for the measured T_i data.

A comparison of the different power terms contributing to the energy balance shows that the heat conductivity term is dominant in the plasma centre, and that at the plasma edge ion energy is predominatly lost by charge exchange (see Figs. 6a to 8a). With increasing central density, P_{ei} approaches the ohmic heating power P_{OH} but stays well below it. P_{ei} increases with radius from the plasma centre up to r = 6 cm. For r > 6 cm P_{ei} decreases because both measured and calculated T_i values are above the experimental T_e values so that energy flows back from the ions to the electrons.

IV.2 Power balance for case IA-6.2

Because of reduced gas input, the density is lower in this case when disruption occurs after impurity accumulation. In order to explain the experimental T_i profiles, the heat conductivity coefficient of Galeev and Sagdeev has to be moderately increased (see Figs.9 to 11). The coefficient of Hazeltine and Hinton, however, has to be increased by a factor of about 5 at low density and a factor of 3 at high density to give agreement with the central ion temperature.

A comparison of the different terms in the power balance shows that the increase of the heat conductivity term from 60 ms to 90 ms is mainly caused by the rising ion-temperature with density. Though the neutral-gas density in the plasma centre decreases with time, the dominant loss term at the boundary P_{cx} increases with density owing to the increase of neutral gas density at the plasma edge (see Fig.2).

At 60 ms, P_{ei} levels out at the plasma edge. T_i does not rise above T_e for all radii. At 80 ms P_{ei} shows a maximum at 6 cm. For r > 6 cm one has $T_i > T_e$. This dependence of P_{ei} is even more pronounced at 90 ms, where P_{ei} shows a sharp maximum at r = 5 cm. The reason for the rise of T_i in the outer plasma zones is probably due to the improved heating of the outer

plasma zones from the plasma core as a consequence of the increasing ion heat conductivity with density. Even if the details of the radial dependence of P_{ei} are somewhat uncertain owing to uncertainties in the measured T_i values at the plasma edge and owing to the extrapolation of T_e data beyond $r = 8$ cm, the above-mentioned tendency is even more pronounced if P_{ei} is calculated from experimental T_i data.

$T_i > T_e$ in the outer zones is possible for ohmic heated plasmas when the high ion heat conduction is responsible for heating the ions at the plasma edge and possibly the electrons there, too. The fact that energy is circulated from the electrons to the ions in the plasma core, transported from there to the plasma outer zones by ions owing to their high heat conductivity, and there partly transferred back to the electrons is also borne out by considering the total power radiated from the electrons. In some cases, at high density practically the full ohmic power is transferred to the ions in the region $r < 5$ cm, which corresponds to 65 % of the total ohmic power. But, nevertheless, it is observed that about 50 % of P_{OH} are lost by radiation mainly via impurity lines located at the plasma edge /12/. Thus, considerations on the bolometically measured signals are in favour of the condition $T_i > T_e$ at the plasma edge zones.

However, it is impossible for a plasma which is just ohmically heated that the integral value P_{ei} becomes negative as is the case for 90 ms for $r > 7.5$ cm(see Fig.11b) if experimental T_i data are used to calculate P_{ei}. A similar dependence of P_{ei} is reported for TFR, too, and tentatively explained by an anomalous heat term /5/. In the case of Pulsator this observation raises doubts about the accuracy of the T_i values measured at the plasma edge. This will be further discussed in Sec.IV.10 (see also Ref. /13/).

IV.3 Power balance for case LC

Figures 12 to 14 show the ion temperature profiles and the ion power balance at three different times during the low current and low toroidal field discharge. The heat conductivity coefficient of Hazeltine and Hinton has to be increased by 2 to reproduce the central T_i data, while the heat conductivity coefficient of Galeev and Sagdeev does not have to be enhanced. Ion heat conduction of this discharge type is approximately neoclassical.

IV.4 Power balance for case DL

This case differs from the previously discussed cases since even the heat conductivity coefficient of Galeev and Sagdeev has to be increased by a factor of 2 to 3 to account for the experimental data. The heat conductivity coefficient of Hazeltine and Hinton must be multiplied by 4 to 5 (see Figs.15 to 18) at low density.

From the point of view of ion heat transport, this type of discharge seems to deviate from the above-discussed cases as a heat conductivity coefficient slightly above the neoclassical value is required to match the experimental data. From the cases considered here, case DL is not the one with the highest electron density or the highest $\partial E_i/\partial t$. This case therefore does not require the highest correction terms in T_i or in the energy input to the ions. Furthermore, the heat conductivity coefficient has to be increased more at low density and less at high density. At low density, however, the ion temperature can be determined with less correction and higher accuracy than at high density (drift effects due to toroidal field ripple do not play a role in Pulsator; see Ref./14/).It seems, that the high heat conductivity found in this type of discharge is beyond experimental uncertainties.

Figure 18 shows that at 80 ms P_{ei} is, experimentally, not to be distinguished from P_{OH} for $r < 5$ cm. Within this volume the available power P_{OH} flows via the electrons to the ions. (Within the error bars, this is not in contradiction to the weak electron losses due to the still present internal disruption to which an energy confinement time of 25 ms can be attributed, which is equivalent to 10 % of P_{OH}.) At the prevailing high ion losses the limitation in T_i shown in Fig.4a compared with the time dependence of T_i of discharge IA-8.7 seems to be a consequence of the limitation in the available power for the ions which, in this particular case, is P_{OH}. The observation of a low electron temperature of 550 eV for case DL compared with 610 eV to 640 eV for case IA-8.7 supports the conclusion of a heavy power loss of the electrons.

IV.5 Power balance for case HC

Most important in investigating the power balance of this high-current low q discharge is the result that very high multiplication factors for the ion heat conductivity coefficients are required at low density to match the experimental T_i data at the plasma centre (see Figs.19 to 23). It is noteworthy that the enhancement factor α decreases with density and at the highest densities neoclassical heat conductivity is approached.
Though the electron density in the plasma centre is $1.9 \times 10^{14} cm^{-3}$ at 85 ms, in this case P_{ei} stays well below the ohmic heating term for all radii, this being in agreement with the heavy sawtooth activity of this low-q discharge.

IV.6 Power balance for case LD

To illustrate the differences to a high-density discharge, the ion power balance is analyzed for a low density discharge, too (see Fig.24). The measured central ion temperature is 150 eV. This value is somewhat higher than the T_i data shown in Fig.4a obtained at low density without additional gas input. The difference is presumably due to a somewhat higher electron density.

Figure 24 shows the central value of T_i together with the calculated T_i profile. Agreement is obtained by increasing the heat conductivity coefficient of Hazeltine and Hinton by a factor of 3.

The power balance in this case is dominated by the approximately equal terms of charge exchange and particle diffusion and to a lesser extent by heat conductivity.

IV.7 Effect of density build-up in the plasma centre on the ion power balance

In common with other tokamaks run at high density, the value of n_o in the plasma centre cannot locally explain the density build-up there even if ionization of partly excited H_o states and the increase of the neutral gas density at the limiter and the location of the gas input as experimentally observed /14/ are considered.

It has been proposed that the density build-up in the plasma centre is supported by a particle current directed inward owing to the trapped particle pinch effect /15/. With a particle current directed to the plasma centre there is a heat current given by $P_c = \frac{3}{2} \frac{1}{r} \frac{\partial}{\partial r} (r\, n_i\, v\, T_i)$. The power balance (eq. (2)) is supplemented by this term in the range where

ionization of the neutral-gas density is insufficient to account for the experimentally observed density rise. The velocity of the particle drift to the plasma centre is determined from

$$v(r) = r^{-1} n_e^{-1} \int \left(\frac{dn_e}{dt} - n_e n_o X_{ei}\right) r\, dr$$

By adding this term to the power balance the central value of T_i increases by ~5% compared with the previous results obtained from solving eq.(2). This difference is well within experimental uncertainties and does not modify the previous results and conclusions.

IV.8 Ion heat conductivity coefficient

The radial dependence of experimental values for the ion heat conductivity χ_i at 80 ms are plotted in Fig.25a for discharge IA-8.7 and in Fig.25b for discharge DL. χ_i is determined from

$$\chi_i(r) = \frac{P_{ei} + P_{iz} - \frac{\partial E_i}{\partial t} - P_{cx} - P_D}{4.4 \times 10^{-16} r n_i \frac{dT_{iexp}}{dr}} \qquad (6)$$

using experimental T_i profiles for evaluating the different terms in the numerator of eq.(6). No determination of χ_i is carried out for $r > 6$ cm because heat conduction loses its dominance as leading term of the energy balance. The data points are compared with the radial dependence of χ_i calculated from the neoclassical relation of Hazeltine and Hinton (eq.(3)) and Galeev and Sagdeev (eq.(5)), respectively. For case IA-8.7 there is fairly good agreement with both calculated coefficients. For case DL the data points are well above the neoclassical coefficients. The data points do not indicate an increase of χ_i at small radii, as the heat conductivity coefficient of Hazeltine and Hinton does.

The data points rather stay constant as expected from the coefficient of Galeev and Sagdeev. But as the uncertainties in the evaluation of χ_i rise to small radii no clear conclusion can be drawn from this comparison.

Figure 26 shows the variation of $\chi_i \times T_i^{3/2}$ with density. χ_i is determined at r = 4 cm for discharge IA-8.7 and discharge DL. Within the error bars there is no variation of χ_i with density. This is in agreement with neoclassical theory. Again there is clear correspondence to the coefficient of Galeev and Sagdeev (dashed curves) than that of Hazeltine and Hinton (solid curves).

From the ion temperature profiles shown in Figs.6 to 24 and from the results plotted in Figs.25 to 26 it has to be concluded that the heat conductivity coefficient observed in Pulsator is slightly above the neoclassical value but generally within the limits with which the neoclassical coefficients can be determined. However, better agreement with the coefficient of Galeev-Sagdeev than the coefficient of Hazeltine-Hinton is observed. There are cases, however, at which the heat conductivity is far above the neoclassical values thus, indicating the occurrence of anomalous ion heat conduction.

Figure 27a shows the enhancement factor α by which the heat conductivity coefficient of Hazeltine and Hinton has to be increased in order to fit the calculated T_i profiles to the central T_i values, as shown in Figs.6c to 24c for the different discharge types. Discharge HC most clearly deviates from the other cases. At low density a heat conductivity coefficient is observed which is a factor of 10 above the neoclassical value. An anomalous ion heat conduction like this has hitherto only been reported for TFR discharges (Ref./5/). For these cases for which α is well above 2,

which is roughly the accuracy limit of the neoclassical coefficients, α decreases with increasing density and approaches the neoclassical limit. This is again most clearly documented by the high-current discharge HC. Contrary to this, the low-current discharge LC shows marginally neoclassical ion transport.

It is tempting to conclude from the results shown in Fig.27a that there is anomalous ion transport excited at high plasma current density which decreases to the neoclassical limit at high plasma density.

From the enhancement factor α and the neoclassical heat conductivity coefficient an anomalous heat conductivity coefficient χ_{AN} can be calculated. In Fig. 27b χ_{AN} obtained at r = 4 cm is plotted versus electron density for discharge HC. The data points are compared with the anomalous particle diffusion coefficient D_{AN} as given in Ref. /18/.

$$D_{AN} = 2.5 \times 10^{19} / (n_e q \, T_e^{3/4})$$

There is rough agreement between the absolute values of χ_{AN} and D_{AN}. Furtheron, the variation of D_{AN} with n_e and q might explain the observed density dependence of α and qualitatively the observation that the highest enhancement factors are required for discharge HC where q is lowest.

The comparison between D_{AN} and the data points suggests that the power contribution due to particle diffusion might be underestimated in eq. 2 and that the anomalous cases observed are predominantly caused by anomalous particle diffusion and not by anomalous heat conductivity.

IV.9 Collisionality

As shown in Fig.6b to 24b for the different discharges the collisional parameter ν (eq.(4)) is a strong function of the plasma radius. In the plasma centre the ions are deep in the plateau regime. To the plasma edge collisionality increases and the collisional regime is reached. For comparison, ν is calculated from the calculated T_i profile with enhanced heat conductivity coefficient (solid curve) and the experimental T_i data (dashed curve).

Because of the increase of T_i and the decrease of Z_{eff} with density, collisionality in the plasma core does not change drastically with gas input. Generally, collisionality increases somewhat during the density build-up.

IV.10 Width of experimental T_i profiles

A comparison of the measured T_i profiles with the calculated T_i profiles show that the experimental profiles are generally broader. There is some doubt that the experimental T_i values at the plasma edge reflect the temperature of the majority of plasma ions there. It is shown in Ref./13/ that backscattering from the vessel wall can dominate the flux spectrum at the plasma edge thus, simulating higher T_i values. In analyzing the data presented here,we have tried to circumvent the effect of backscattering by properly choosing the energy interval in the neutral spectrum from which T_i is deduced. But still the T_i profiles remain broader than expected. There are three experimental indications with show that the actual T_i profile may be closer to the calculated T_i profile at the plasma edge.

- With the calculated T_i profile put into eq.(1) there is generally better agreement with the experimentally observed flux spectrum in the low-energy range between 100 to 800 eV compared with the spectrum calculated with the T_i profile actually measured.

- Plotted in Figs. 17 and 18 are two ion temperature values measured with Doppler broadening of O^{V} and O^{VI} lines. The data are somewhat lower than the charge exchange points[+].

- P_{ei} calculated from the experimental T_i data occasionally becomes negative at the plasma edge. This is not possible for ohmically heated plasmas.

Because of this uncertainty, energy confinement times discussed in the following section are determined from calculated T_i profiles adjusted to the central values of the measured T_i data by enhancing the heat conductivity coefficient as described above. Generally, there is good agreement between measured T_i data and calculated profiles for $r \lesssim 6$ to 8 cm.

V. Ion energy and electron energy confinement times

The ion energy confinement time is calculated from

$$\tau_{Ei}(r) = \frac{\frac{3}{2}\int_0^r n_i(r')T_i(r')r'dr'}{P_{in}(r)} \qquad (7)$$

P_{in} is the total input power to the ions corrected by the term $\partial E_i/\partial t$. In the plasma interior, P_{in} is given by P_{ei}. In the plasma edge zones, generally $T_i > T_e$ at high density. In these cases P_{in} is given by P_{HC} and in some cases by P_D contributions.

The electron energy confinement time is given by

$$\tau_{Ee}(r) = \frac{\frac{3}{2}\int_0^r n_e(r')T_e(r')r'dr'}{P_{OH}(r) - P_{ei}(r)} \qquad (8)$$

In this case, a correction due to the time dependent term in the electron energy balance $\frac{\partial E_e}{\partial t}$ can be neglected since the electron temperature T_e decreases with increasing electron density.

Figures 28 to 30 show the radial dependence of τ_{Ei} and τ_{Ee} for discharges IA-8.7, IA-62. and HC. Plotted are results for different phases during the discharge with the plasma density increasing.

[+] The Doppler broadening measurements were made by W.Engelhardt

In the plasma centre, internal disruption is one mechanism which limits electron energy confinement. The energy confinement time τ_{e}^{SS} from internal sawtooth is calculated from /16/:

$$\tau_{e}^{SS} = \frac{2}{3} \frac{a^2}{r_1^2} \Delta t \qquad (9)$$

a = limiter radius, r_1 = radius of q=1 surface, Δt = sawooth period. The values of τ_{e}^{SS} are plotted in Figs.28 to 30 as straight lines which end at the radius of the q=1 surface.

At low densities one has $\tau_{Ei} \sim (2\text{-}4)\tau_{Ee}$. The dominant plasma energy losses are via the electrons. Within the error limits, τ_{Ee} does not vary with radius, this being a consequence of $T_e(r) \propto (n_e(r))^2$.

With increasing density τ_{Ee} assumes a strong dependence on the plasma radius. While the total value $\tau_{Ee}(a)$ increases moderately the central value $\tau_{Ee}(0)$ increases steeply with density. τ_{Ei} shows the opposite dependence. τ_{Ei} decreases with density at all radii. At high density $\tau_{Ei} < \tau_{Ee}$ in the plasma interior. Now, plasma energy losses from the core are predominantly via the ions.

At low density, $\tau_{Ee}(0)$ is well below τ_{e}^{SS}, thus, indicating additional loss mechanisms to sawtooth oscillations for the electrons. With increasing density, $\tau_{Ee}(0)$ approaches τ_{e}^{SS}. Within the estimated uncertainty of the experimental data, at high density $\tau_{Ee}(0)$ seems to be limited by internal disruption as dominant electron loss process. Interesting to note is the radial dependence of $\tau_{Ee}(r)$. At high density there is a plateau in $\tau_{Ee}(r)$, or $\tau_{Ee}(r)$ even increases up to a radius which is comparable with the radius of the q=1 surface.

Most remarkable, however, is the behaviour of $\tau_{Ee}(0)$ in those discharges (IA.8.7 and IA-6.2) where q(0) increases above 1 so that internal disruption stops and impurity accumulation occurs. This happens in discharge IA-8.7 from 70 ms to 80 ms.In Figs.28c and d $\tau_{Ee}(r)$ is plotted versus the radius with internal disruption at 70 ms and without

internal disruption at 80 ms. The two curves for τ_{Ee} are the results of the same type of discharge measured at two different days. Both show a steep increase in $\tau_{Ee}(0)$ as soon as internal disruption has stopped. $\tau_{Ee}(0)$ increases from an average of 13 ms, this low value being due to internal disruption, to about 22 ms, this value being limited by another loss mechanism. Radiation by these impurities which have migrated to the plasma centre accounts for $\sim$ 1/3 of the total energy lost from the plasma centre by electrons.

The improvement of electron energy confinement by cessation of internal disruption can also be seen from discharge IA-6.2. This discharge is totally different concerning density build-up and density limit but it also shows the phenomenon of impurity accumulation. At 80 ms $\tau_{Ee}(0)$ is 9 ms and obviously limited by internal disruption. At 90 ms, internal disruption has stopped and $\tau_{Ee}(0)$ has risen to 14 ms.

Figure 31 summarizes the obvious effect of internal disruption on the radial variation of $\tau_{Ee}(r)$. Plotted are $\tau_{Ee}(r)$ of discharge IA-8.7 at 80 ms and discharge HC at 65 ms. The peak electron density $n_e(0) = 1.4 \times 10^{14} cm^{-3}$ and $Z_{eff} \sim 2$ are the same for both discharges. $\tau_{Ee}(r)$ is plotted for both cases, once using the T_i profile as calculated from the ion energy balance equation adjusted to the experimental values (solid curves) and, for comparison, using the experimental T_i profile (dashed curves). Discharge IA-8.7 does not show internal disruption at 80 ms, while discharge HC shows intense internal sawtooth activity. The sawtooth modulation of the central X-ray diode is 30 to 40 %.
Within the assumed error bars, τ_{Ee} is approximately the same for both discharges in the range from 6 cm to the limiter but different for $r < 6$ cm. In discharge IA-8.7 τ_{Ee} continues to rise to 25 ms at $r = 0$, and τ_{Ee} of discharge HC has a maximum at 6 cm and decreases to 13 ms at $r = 0$. $\tilde{\tau}_e$ attributable to internal disruption is calculated from eq.(8) to be 9 ms. The radius of the $q = 1$ surface for discharge HC is 4 cm. The ob-

servation of a maximum in τ_{Ee} at r = 6 cm $\simeq \sqrt{2} \cdot r_1$ is in rough agreement with considerations concerning the radial extent of electron heat transport due to internal disruption /16/.

The heat conductivity $\chi_e^{\prime\prime}$ attributable to internal disruption can be deduced from the sawtooth repetition time Δt:

$$\chi_e^{\prime\prime} = \frac{3}{8} \frac{r_1^2}{\Delta t} .$$

For the case shown in Fig.31 $\chi_e^{\prime\prime}$ is estimated to $3 \times 10^3 cm^2 s^{-1}$. The corresponding power $P_e = 2.6 \times 10^{-15} n_e \chi_e^{\prime\prime} \partial T_e / \partial r$ transported by the electrons by internal disruption through the r = 6 cm surface is $\sim 10^5$ W and compares well with the 1.7×10^5 W deposited by ohmic heating within the volume bounded by r = 6 cm and 9×10^4 W transferred to the ions.

$\tau_{Ee}(r)$ of discharge DL and LC show the familiar behaviour of the already discussed discharges. At low density, τ_{Ee} is approximately a factor of 2 to 4 lower than τ_{Ei} and is independent of radius. With increasing density τ_{Ee} increases for all radii, but again more steeply for the central values. For these discharges $\tau_{Ee}(0)$ seems to be limited by internal disruption indicated by a maximum of τ_{Ee} between r = 3 cm and 5 cm. In discharge DL, P_{ei} approaches P_{OH} with the consequence that $\tau_{Ee}(0)$ becomes a badly determined quantity owing to uncertainties in T_i and T_e.

Figures 32a and b show the variation of $\tau_{Ee}(0)$ with the central electron density and of the global value $\tau_{Ee}(a)$ with the mean electron density, respectively. As a reference the dashed lines indicate proportionality to density. The $\tau_{Ee}(a)$ values indicate saturation at high density. Discharge HC shows the shortest electron energy confinement time corollary of the intense sawtooth activity of this discharge.

Typical of all discharge types is that the ion energy confinement time τ_{Ei} increases with radius up to r = 6 to 8 cm. Beyond this radius τ_{Ei} decreases. One has to bear in mind, however, that in this range of the plasma τ_{Ei} is a poorly determined quantity because both T_e and T_i are not known accurately enough and only slightly different. The increase in τ_{Ei} with radius may be due to the decreasing heat conductivity. The decrease of τ_{Ee} at the plasma edge may reflect the increasing charge exchange ion losses.

Figures 33 and 34 show the variation of the central value $\tau_{Ee}(0)$ with peak electron density and the dependence of the global value $\tau_{Ei}(0)$ on the average electron density. τ_{Ei} decreases with density for all discharge types apart from discharge HC. In this case, τ_{Ei} practically does not change with density. The cause for this different behaviour may be the interaction of two separate factors with different density dependence. First neoclassical heat conductivity losses increase with density, thereby decreasing τ_{Ei}. But as seen in Sec. IV.8, the heat conductivity of discharge HC is characterized by an enhancement factor which decreases with density. Both factors may cause τ_{Ei} of this discharge to remain roughly independent of density.

Figure 35 shows the dependence of the product $\tau_{Ei}(0) \times T_i(0)^{3/2}$ on the peak electron density $n_e(0)$. No density dependence can be detected within the scatter of the data. $\tau_{Ei} \propto T_i^{-3/2}$ without any density dependence is expected from neoclassical theory for a plasma in the plateau regime. This dependence implies, too, that ion energy confinement in Pulsator is limited by heat conduction and, contrary to the electrons at high density, not by internal sawtooth. The lack of density dependence of τ_{Ei} shows that the effective density variation demonstrated by Figs.33 and 34 is actually caused by the ion temperature increase with density.

Figures 36a and b show the global transport coefficient calculated from the confinement times $\tau_{Ei}(a)$ and $\tau_{Ee}(a)$ using: $\chi_i = a^2/4\,\tau_{Ei}(a)$ and $\chi_e = a^2/4\,\tau_{Ee}(a)$ as a function of the mean electron density. The transport coefficients determined from the global confinement times can be used to generally characterize the transport characteristics governing a discharge. For comparison the dependence $\chi_e = 5 \times 10^{17} n_e^{-1}$ quoted for PLT and Alcator /17/ is plotted in Fig.36a. For $\bar{n} > 6 \times 10^{13}\,cm^{-3}$ one has $\chi_i > \chi_e$. Owing to the ion temperature increase with density for $\bar{n} > 6 \times 10^{13}\,cm^{-3}$ energy transport is dominated by ions with a transport coefficient close to the neoclassical value at high density.

In conclusion, during a high-density discharge in Pulsator, there is a transition from dominant anomalous electron thermal conduction to approximately neoclassical ion thermal conduction. With increasing density, electron thermal conduction decreases and approaches the neoclassical value except in those cases where internal disruption limits the further decrease of χ_e. This is shown in Fig.36a. The data points of χ_e of discharge HC are above the data points of all other discharge types, thus possibly indicating the large sawtooth contribution to electron transport in this specific case. At high density, χ_e of discharge HC seems to level out close to the value $\tilde{\chi}_e$ (see dashed line in Fig.36a) owing to internal disruption, which is calculated from eq.(9).

VI. Particle confinement time

The particle confinement time τ_p can be determined as a function of the radius from the neutral-gas density, assuming particle balance in source and loss terms:

$$\tau_p(r) = \frac{\int_0^r n_e(r')dr' \; r'}{\int_0^r n_e(r')n_o(r') \; X_{ei} \; r'dr'}$$

In Fig.37 $\tau_p(r)$ is shown for a low-density discharge at an electron density of $1.8 \times 10^{13} cm^{-3}$ and a high-density discharge at $1.8 \times 10^{14} cm^{-3}$. The high-density case is evaluated at 110 ms far after gas input at 40 ms so that for both cases $dn_e/dt = 0$. $\tau_p(r)$ is calculated from the two neutral gas density profiles shown in Fig.2 as an insert.

While the central value $\tau_p(0)$ increases from 30 ms to 1000 ms at high density, the global values $\tau_p(a)$ increase from 8 ms to 11 ms. This comparatively weak increase reflects the intense particle recycling at the plasma edge.

Owing to the peculiarities of the gas input in the case analyzed here the assumption of $\frac{dn_e}{dt} = 0$ is justified. $\tau_p(0) = 1$ s for the high density case points out, however, that the assumption of $\frac{dn_e}{dt} = 0$ seriously influences the central value of the particle confinement time. Even a slight increase in density which cannot be resolved experimentally, can cause a negative value of τ_p.

VII. Conclusion

A series of Pulsator discharges has been analyzed for the ion energy balance. Generally, agreement with neoclassical ion transport is observed within a factor of 2 to 3. However, the data agree better with the heat conductivity coefficient of Galeev-Sagdeev than that of Hazeltine-Hinton. Nevertheless, the analysis of the ion energy balance has revealed marked differences between different discharge types. At low plasma density and at high plasma current ion heat transport well above the neoclassical level is observed. The possible occurrence of anomalous ion heat transport seems to increase with plasma current and seems to decrease with increasing plasma density with the heat conduction approaching the neoclassical limit. These observations may indicate that the enhanced ion heat conduction is caused by anomalous particle diffusion and not by anomalous heat conductivity.

During high density build-up there seems to exist a transition from electron-dominated transport from the plasma core to ion--dominated transport. The transition occurs around an average density of $6 \times 10^{13} cm^{-3}$.

Measurements and calculations indicate that $T_i > T_e$ in the outer plasma zones. This observation indicates a circulation of energy. In the plasma interior ions are heated by electrons. Cases are observed at which the power transferred from the electrons to the ions within a radius $r = 5$ cm amount to the total ohmic power deposited within this radius. Owing to the high ion heat conductivity at high density, energy is predominantly transported by ions into the outer plasma zones, thus giving rise to $T_i > T_e$. Conversely, electrons are heated by the ions there. The observation that in high-density discharges, dominated by ion heat conduction, considerable impurity radiation nevertheless occurs may thereby be explained.

It is observed that the electron energy confinement time increases for all radii with density up to a limit in those dis-

charges which exhibit internal disruption. A comparison of electron confinement time profiles of discharges with internal disruption with those without it clearly reveals the limiting effect of internal disruption. The ion energy confinement time decreases with density for all radii and is limited by ion heat conduction.

Acknowledgement

The author whishes to thank S.Sesnic and the Pulsator team for their help and support in the measurements. The ion energy balance as presented here is based on the equilibrium of the electrons. He is particularily indebted to D.Meisel and H.Murmann for providing him with electron density and electron temperature profiles for the different discharges analyzed here. The determination of the energy confinement time due to sawtooth oscillations is based on measurements by S. Sesnic.

The author also wishes to acknowledge the many clarifying discussion with W.Engelhardt, O.Klüber and H.M.Mayer and thank them for helpful contributions and ideas.

Thanks are due to M.H.Hughes for sending a copy of the AURORA code and to A.McKenney for his help in getting the program to run.

The accumulation and processing of all the data was only possible with the excellent technical assistance of G.Riedel and with the data analysis programs written by Miss E.Reimann. Mrs. Volkenandt prepared all the drawings with admirable patience.

References

/1/ Stott, P.E., Plasma Physics 18 (1976) 251

/2/ Brusati, M., et al., Nuclear Fusion 18 (1978) 1205

/3/ Berry, L. A., Phys. Rev. Lett. 32 (1974) 362

/4/ Artsimovich, L.A., et al., JETP Lett. 11 (1970) 304

/5/ Equipe TFR, Nuclear Fusion 18 (1978) 1271

/6/ Engelhardt, W., et al., in Plasma Physics and Controlled Nuclear Fusion Research (Proc. 7th Int. Conf. Innsbruck 1978) Vol. 1, IAEA, Vienna (1979) 123

/7/ Fußmann, G., et al., Proc. 9th Europ. Conf. on Contr. Fusion and Plasma Phys., Oxford (1979), preprint

/8/ Afrosimov, V.V., et al., Sov. Phys. Tech. Phys. 20 (1975) 33

/9/ Hughes, M.H., Post, D.E., Jour. of Comp. Phys. 28 (1978) 43

/10/ Hazeltine, R.D., Hinton, F.L., Phys. Fluids 16 (1973) 836

/11/ Galeev, A.A., Sagdeev, R.Z., Sov. Phys.-JETP 26 (1968) 233

/12/ Müller, R., private communication

/13/ Wagner, F., Mayer, H.M., Proc. 8th Europ. Conf. on Contr. Fusion and Plasma Phys. Vol. 1, Prague (1977) 24

/14/ Wagner, F., Mayer, H.M., Proc. of the Int. Conf.on Plasma Wall Interaction, Jülich (1976) 149

/15/ Ware, A.A., Phys. Rev. Lett. 25 (1970) 15

/16/ Soler, M., Callen, J.D., Nuclear Fusion 19 (1979) 703

/17/ Post, D.E., et al., in Plasma Physics and Controlled Nuclear Fusion Research (Proc. 7th Int. Conf. Innsbruck 1978) Vol. 1, IAEA, Vienna (1979) 471

/18/ Mercier, C., Werkhoff, F. and Morera, J.P., Report EUR-CEA-FC 997 (1979)

/19/ Gondhalekar, A., et al.. preprint, submitted for publication in Nuclear Fusion

/20/ Paul, J.W.M., et al., in Plasma Physics and Contr. Nucl. Fusion Research (Proc. 6th Int. Conf. Berchtesgaden 1976) Vol. 2, IAEA, Vienna (1977) 269

/21/ Berry, L.A., et al., in Plasma Physics and Contr. Nuclear Fusion Research (Proc. 7th Int. Conf. Berchtesgaden 1976) Vol. 1, IAEA, Vienna (1977) 49

/22/ Equipe TFR, in Plasma Physics and Contr. Nuclear Fusion Research (Proc. 7th Int. Conf. Innsbruck 1978) Vol. 1, IAEA, Vienna (1979) 135

/23/ Gorbunov, E.P., et al., in Contr. Fusion and Plasma Physics (Proc. 6th Europ. Conf., Moscow, 1973) Vol. 1, 4

/24/ Bagdasarov, A.A., et al., in Plasma Physics and Contr. Nuclear Fusion Research (Proc. 7th Int. Conf. Innsbruck 1978) Vol. 1, IAEA, Vienna (1979) 135

Table I

Type of discharge	Average density at disruption (cm^{-3})	I_{plasma} (kA)	B_{Tor} (kG)	q(a)	Typical $T_e(0)$ values (eV)	
IA-8.7	8.7×10^{13}	55	27.5	4.3	80 ms: 610-640	Impurity accumulation: during the last 10 ms of the discharge saw-teeth stop and impurities accumulate in the plasma centre
IA-6.2	6.2×10^{12}	55	27.5	4.3	90 ms: 680	
DL	1.12×10^{14}	55	27.5	4.3	80 ms: 550	Density limit: plasma disrupts at density limit
LC	6.5×10^{13}	40	20	4.3	55 ms: 430	Low-current, low-magnetic field discharge
HC	1.32×10^{14}	90	27.5	2.6	85 ms: 550	High-current, low-q(a) discharge with intensive sawtooth at $\Delta T_e/T_e \sim 15$ %
LD	1.2×10^{13}	50	28	4.8	40 ms: 1050	Low-density discharge; no additional gas input

Figure Captions

Fig. 1: Time evolution of the line averaged density for the different discharges analyzed in this report.

Fig. 2: Two examples of measured flux spectra at low and high density, repectively.
Solid curves: calculated spectra from the neutral gas density profiles shown as insert.

Insert: neutral gas density profiles determined from experimental data with the AURORA Monte Carlo Code /Ref.19/.

Fig. 3a: Variation of the neutral gas density in the plasma centre with the line averaged electron density.

3b: Variation of the ratio of central neutral gas density to edge neutral gas density with the line averaged electron density.

Fig. 4a: Time evolution of the ion temperature of discharge types HC, LC and IA-6.2. These high-density discharges are compared with a typical low-density discharge (LD) without additional gas input.

4b: Time evolution of the ion temperature of discharges DL and IA-8.7.

Fig. 5: Time evolution of the particle fluxes at 1500 eV during the high-density discharges DL and IA-8.7.

Figs.6-24:

a: Plotted are the different power contributions to the ion energy balance calculated from the ion temperature profiles obtained from solving the ion energy balance equation. The neoclassical ion heat conductivity coefficient of Hazeltine and Hinton is enhanced in order to reproduce the experimental central T_i data

P_{OH} = ohmic heating power

P_{ei} = power transferred by electron-ion collisions

P_{cx} = power lost by charge exchange

P_D = power lost by particle diffusion

P_{HC} = power lost by ion heat conduction

P_{iz} = power gained by neutral ionization

$P_{PL} = \partial E_i / \partial t$ = power stored within the plasma

b: Ion collisionality parameter ν versus plasma radius for the calculated T_i profile (solid curve) and the experimental T_i profile (dashed curve). The two dotted dashed curves give the boundary between the plateau regime and collisional- or collision-free-regime, respectively.

c: Plotted are measured ion temperature profiles for the different discharge types. The solid curves are calculated ion temperature profiles obtained by solving the ion energy balance with the use of the heat conductivity coefficient of Hazeltine and Hinton. The dashed curves are obtained by using the heat conductivity coefficient by Galeev and Sagdeev. The heat conductivity coefficients are enhanced by the factor given at the curves.
For discharge type LC (shown in Figs.12 to 14) only a half profile of T_i is measured. To facilitate comparison with the theoretical curves, the profile is supplemented by transferring the measured data points of the right branch to the left side to give a full profile.

Fig.11b: Plotted are the different power contributions to the ion energy balance calculated from the experimental ion temperature profile. The heat conductivity term is calculated from Hazeltine and Hinton. The ion energy equation is not balanced in this case. Beyond $r = 7.5$ cm P_{ei} is negative.

Fig.25a,b: Experimental values of the ion heat conductivity for different radii for discharge IA-8.7 (a) and discharge DL (b) at 80 ms. The data points are compared with the theoretical heat conductivity coefficient of Hazeltine and Hinton (solid curve) and Galeev and Sagdeev (dashed cure).

Fig.26: Experimental values of $\chi_i(4) \times T_i(4)^{-3/2}$ determined at $r = 4$ cm versus the electron density at 4 cm. The data points are compared with the neoclassical coefficient of Hazeltine, Hinton and Galeev, Sagdeev.

Fig.27a: Dependence of the enhancement factor α for the heat conductivity coefficient of Hazeltine and Hinton versus the line average electron density.

Fig.27b: Anomalous heat conduction χ_{AN} versus electron density at $r = 4$ cm for discharge HC. The solid line is the anomalous diffusion coefficient $D_{AN} = 2.5 \times 10^{19}/(n_e\ q\ T_e^{3/4})$ of Ref. /18/.

Fig.28-30: Plotted are radial profiles of the ion energy confinement time (solid curve) and electron energy confinement time (dashed curve) for different moments during the discharge. The electron energy confinement time due to sawtooth oscillations $\tilde{\tau}_e$ is plotted as a straight line up to the radius r_1 of the q=1-surface.

In Fig. 28 results of two different runs of discharge type IA-8.7 are plotted at 70 ms and 80 ms.

Fig.31: Radial profiles of electron energy confinement time for discharges HC (dotted curves) and IA-8.7 (solid curves). Peak electron density and Z_{eff} are the same for both discharges. Discharge HC exhibits internal disruption, discharge IA-8.7 is without it. The corresponding confinement time $\tilde{\tau}_e$ is plotted as a straight line up to the radius of the q=1 surface.

One set of curves is obtained from experimental T_i data, the other one by using the calculated T_i profile from the ion energy balance equation with enhanced heat conductivity to match the measured central T_i value.

Fig.32a,b: Central electron confinement time $\tau_{Ee}(0)$ versus peak electron density (a) and global electron confinement time $\tau_{Ee}(a)$ versus average density (b). The dashed lines indicate proportionality to density.

Fig.33: Central ion confinement time versus peak electron density for different discharge types.

Fig.34: Global ion confinement time versus average electron density for different discharge types.

Fig.35: Variation of the product $\tau_{Ei}(0)T_i^{3/2}$ versus peak electron density for different discharge types.

Fig.36a: Plotted is global electron transport coefficient determined from $\chi_e = a^2/4\tau_{Ee}(a)$ versus average line density. The straight line shows the dependence $\chi_e = 5 \times 10^{17}/n_e$ as quoted for PLT and Alcator /17/. $\tilde{\chi}_{e,HC}$ is the thermal conduction attributable to internal disruption of discharge HC.

b: Plotted is a global ion transport coefficient obtained from $\chi_i = a^2/4\tau_{Ei}(a)$ versus average line density. The dashed line indicates proportionality to n_e which, in reality, is caused by the increase of ion temperature with density.

Fig.37: Plotted is the particle confinement time τ_p versus radius for a low-density and a high-density discharge. τ_p is calculated from the neutral-gas density profiles shown as insert to Fig.2.

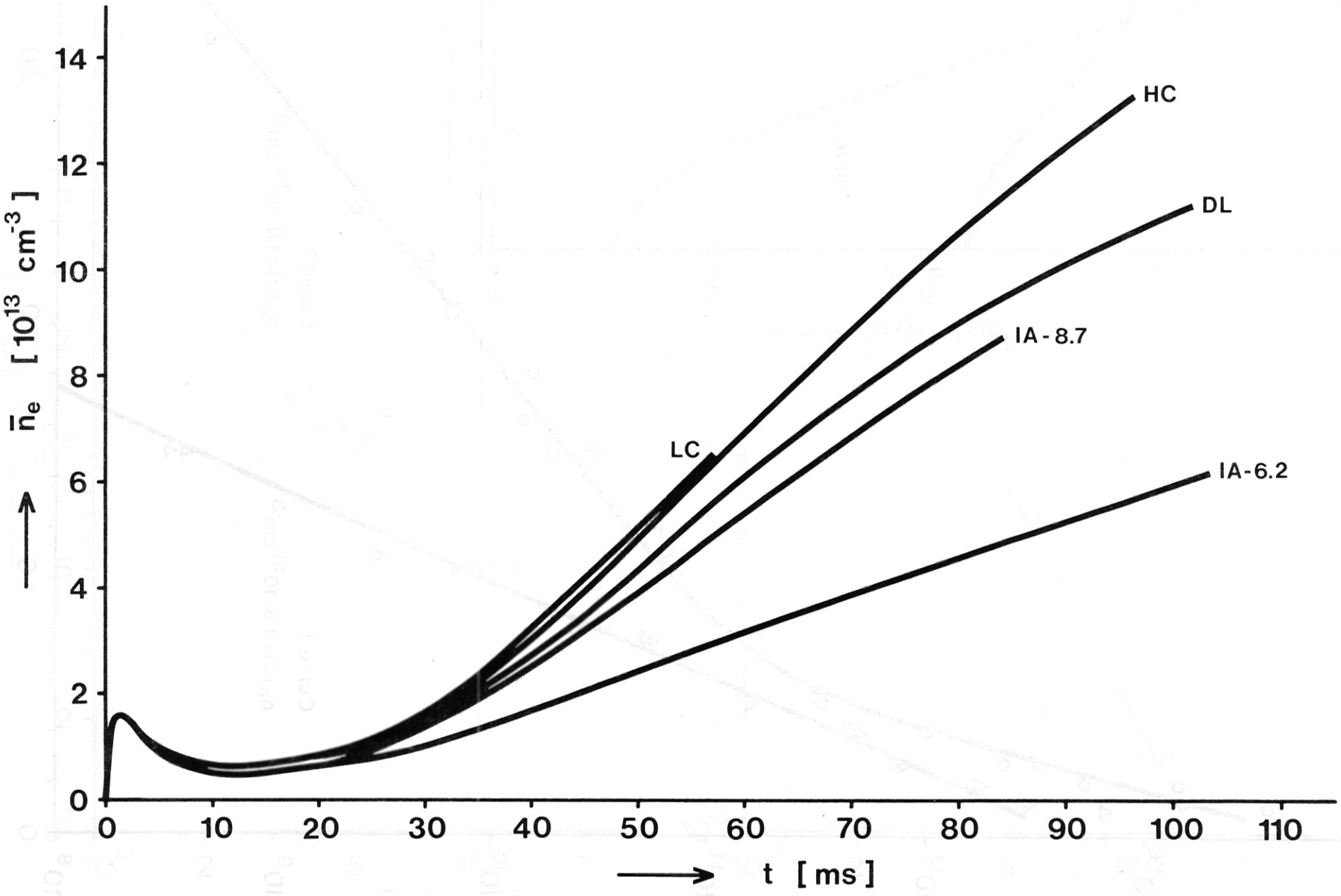
14
12
10
8
6
4
2
0
$\bar{n}_e$ [10^{13} cm^{-3}]
HC
DL
IA-8.7
LC
IA-6.2
0
10
20
30
40
50
60
70
80
90
100
110
t [ms]

Fig. 1

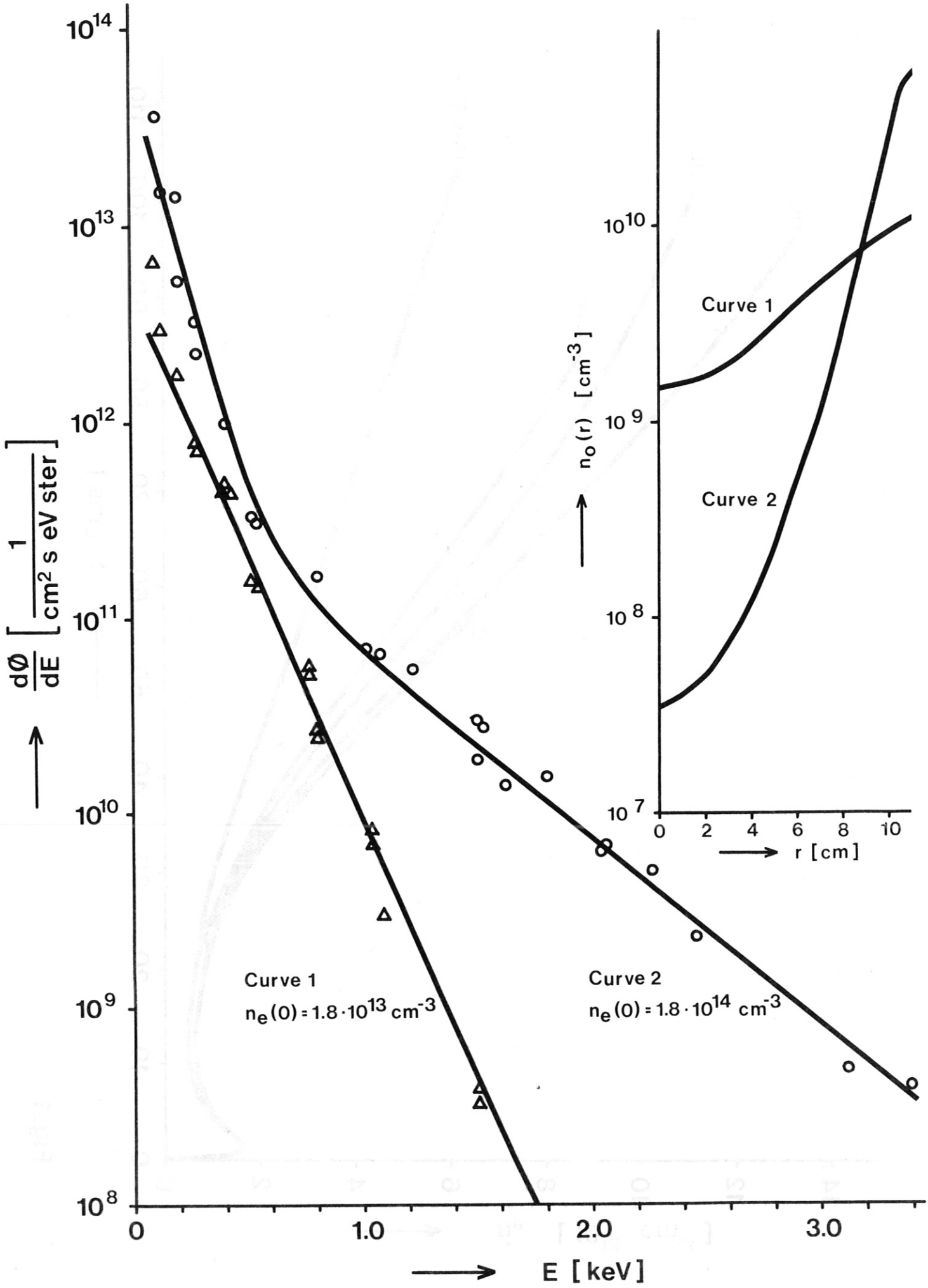
10^{14}
10^{13}
10^{12}
10^{11}
10^{10}
10^{9}
10^{8}
$\frac{d\Phi}{dE}$ [$\frac{1}{cm^2\ s\ eV\ ster}$]
0
1.0
2.0
3.0
E [keV]
Curve 1
$n_e(0) = 1.8 \cdot 10^{13}\ cm^{-3}$
Curve 2
$n_e(0) = 1.8 \cdot 10^{14}\ cm^{-3}$
10^{10}
10^{9}
10^{8}
10^{7}
$n_o(r)$ [cm^{-3}]
Curve 1
Curve 2
0
2
4
6
8
10
r [cm]

Fig. 2

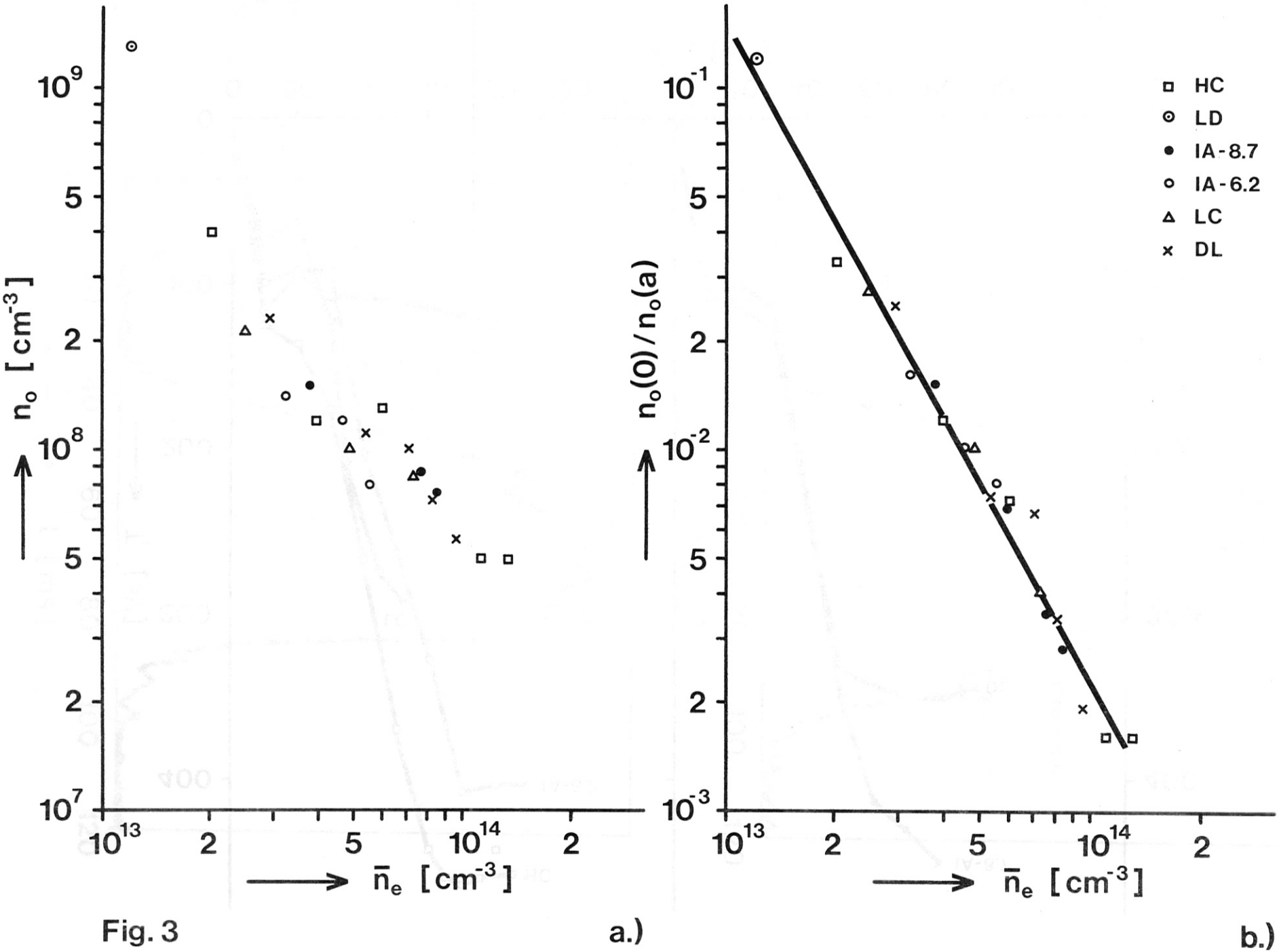
10^9
5
2
10^8
5
2
10^7
n_o [cm^{-3}]
10^{13}
2
5
10^{14}
2
$\bar{n}_e$ [cm^{-3}]
a.)
10^{-1}
5
2
10^{-2}
5
2
10^{-3}
$n_o(0)/n_o(a)$
10^{13}
2
5
10^{14}
2
$\bar{n}_e$ [cm^{-3}]
HC
LD
IA-8.7
IA-6.2
LC
DL
b.)

Fig. 3

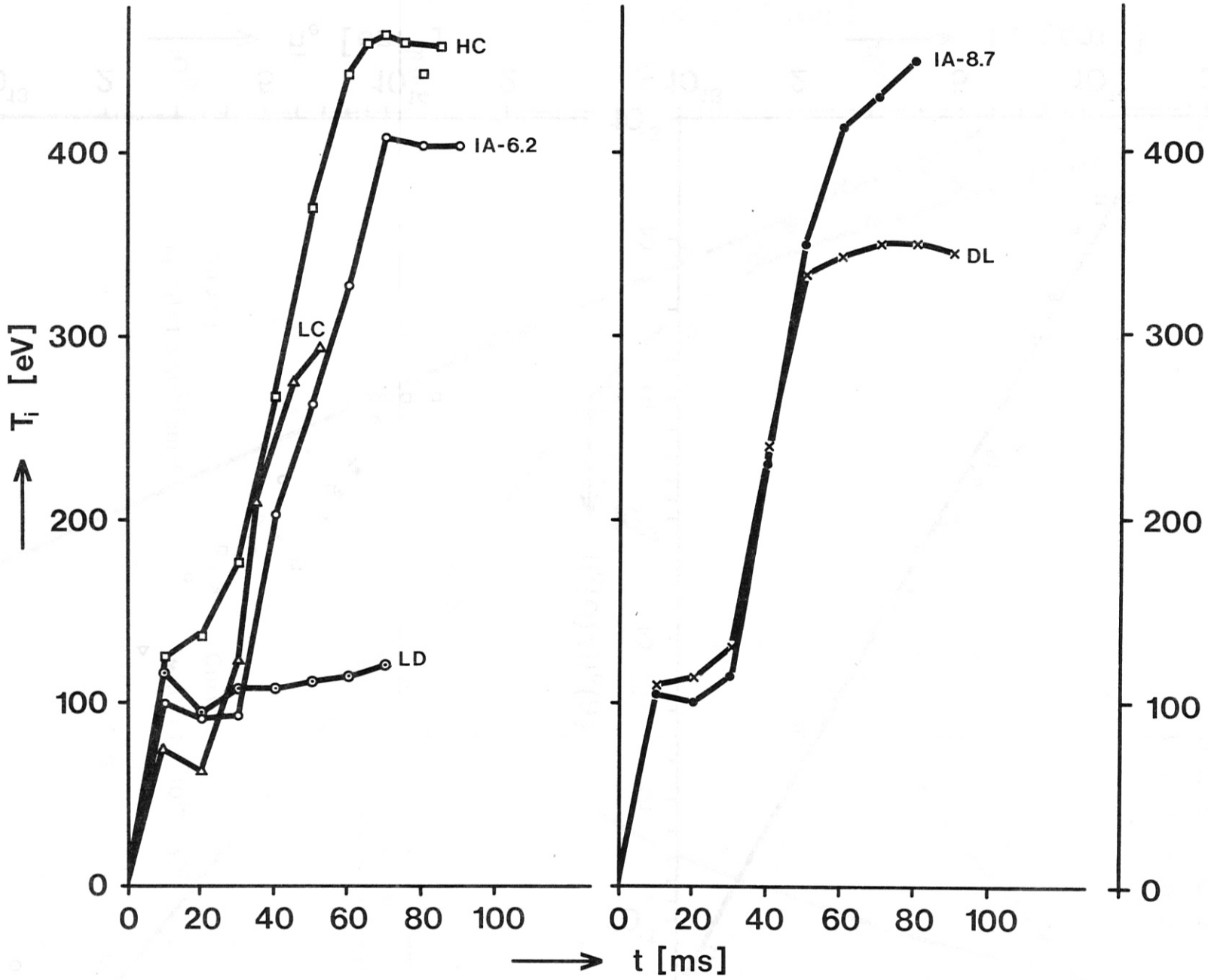
HC
IA-6.2
LC
LD
IA-8.7
DL
T_i [eV]
0
100
200
300
400
0 20 40 60 80 100
t [ms]
a.)
b.)

Fig. 4

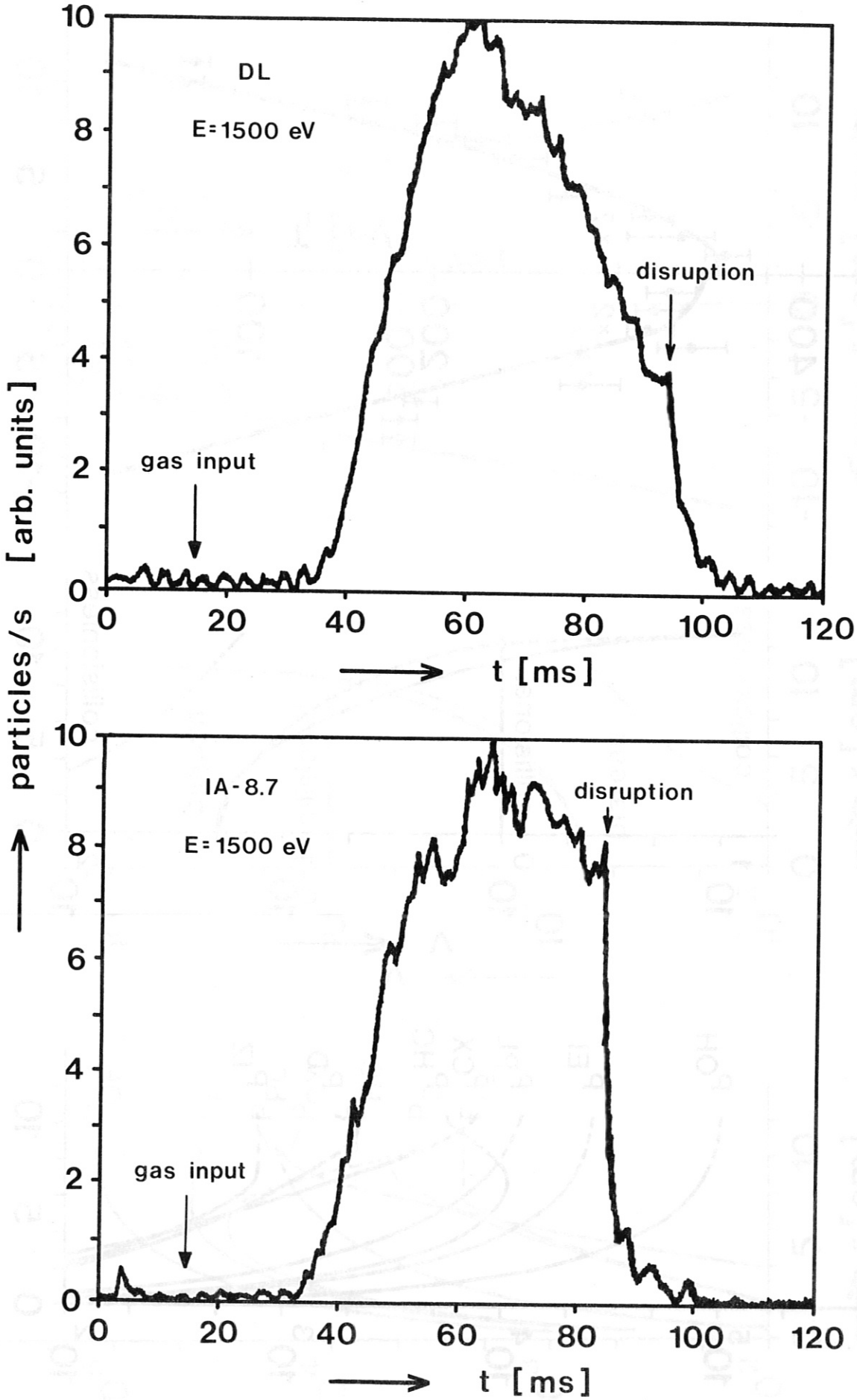
DL
E=1500 eV
disruption
gas input
particles/s [arb. units]
t [ms]
IA-8.7
E=1500 eV
disruption
gas input
t [ms]

Fig. 5

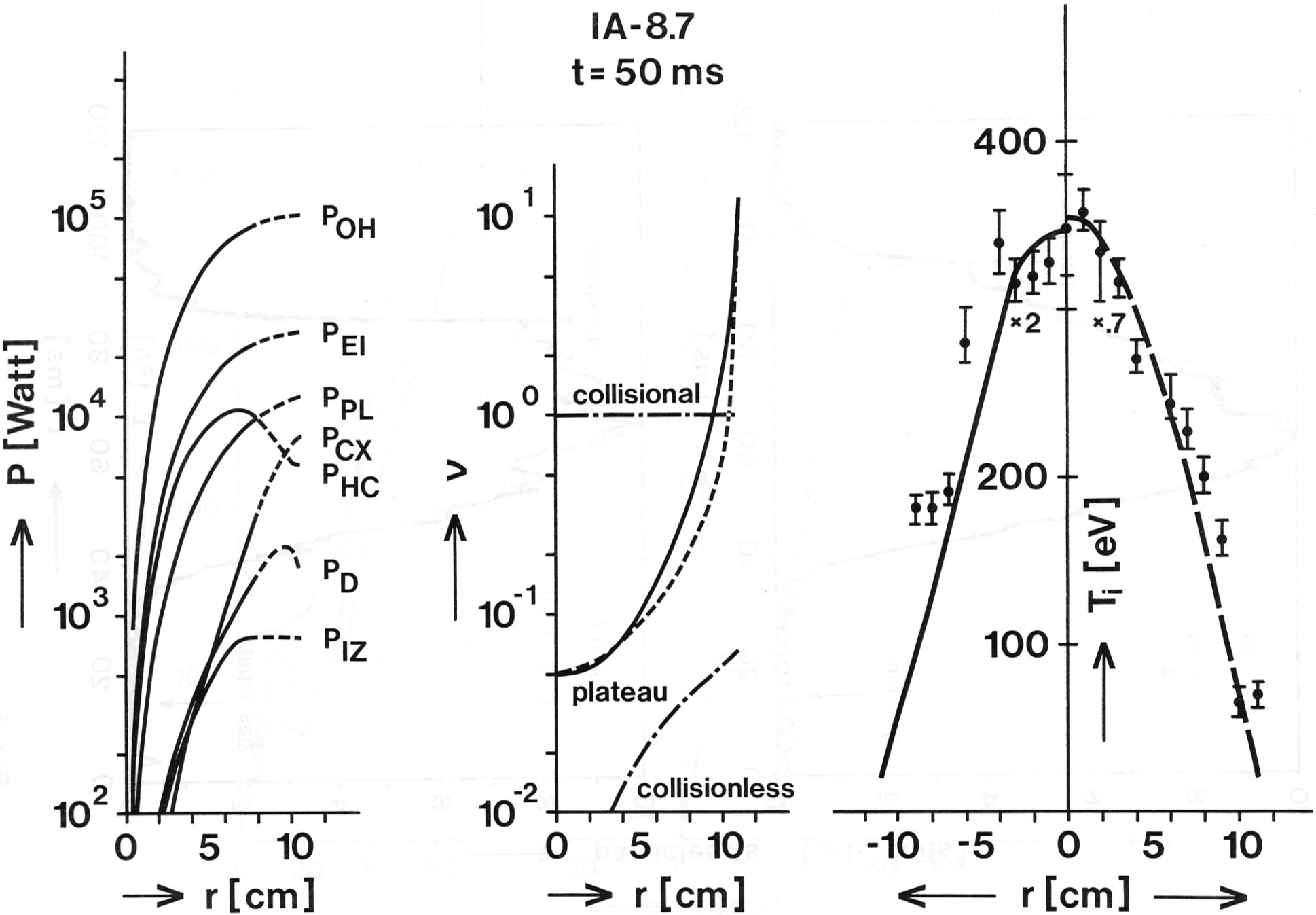
IA-8.7
t = 50 ms
P [Watt]
10^5
10^4
10^3
10^2
P_{OH}
P_{EI}
P_{PL}
P_{CX}
P_{HC}
P_D
P_{IZ}
0 5 10
r [cm]
ν
10^1
10^0
10^{-1}
10^{-2}
collisional
plateau
collisionless
0 5 10
r [cm]
400
200
100
T_i [eV]
×2
×.7
-10 -5 0 5 10
r [cm]

Fig. 6 a-c

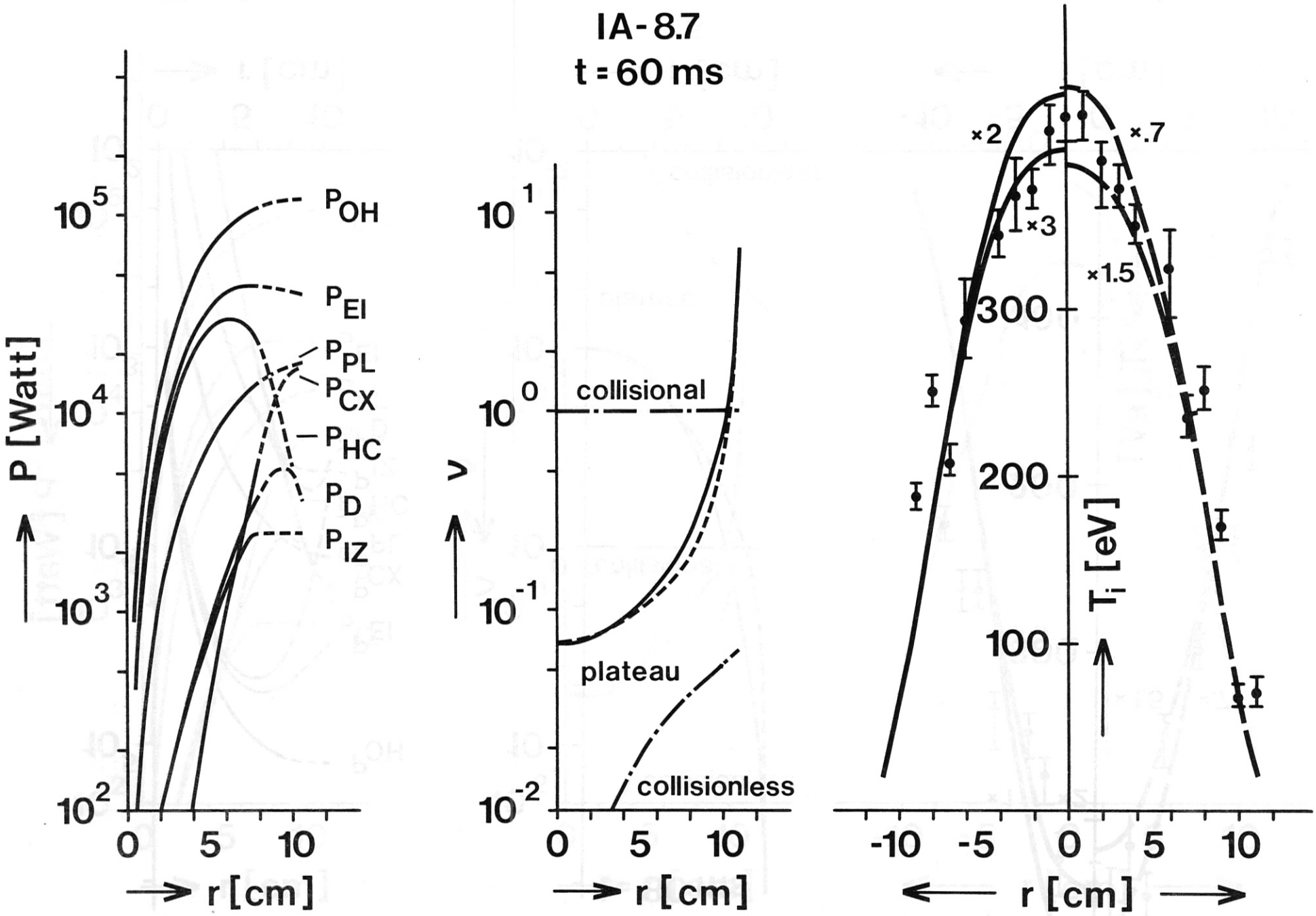
IA-8.7
t = 60 ms
P [Watt]
10^5
10^4
10^3
10^2
P_{OH}
P_{EI}
P_{PL}
P_{CX}
P_{HC}
P_D
P_{IZ}
0 5 10
r [cm]
ν
10^1
10^0
10^{-1}
10^{-2}
collisional
plateau
collisionless
0 5 10
r [cm]
×2
×.7
×3
×1.5
300
200
100
T_i [eV]
-10 -5 0 5 10
r [cm]

Fig. 7 a-c

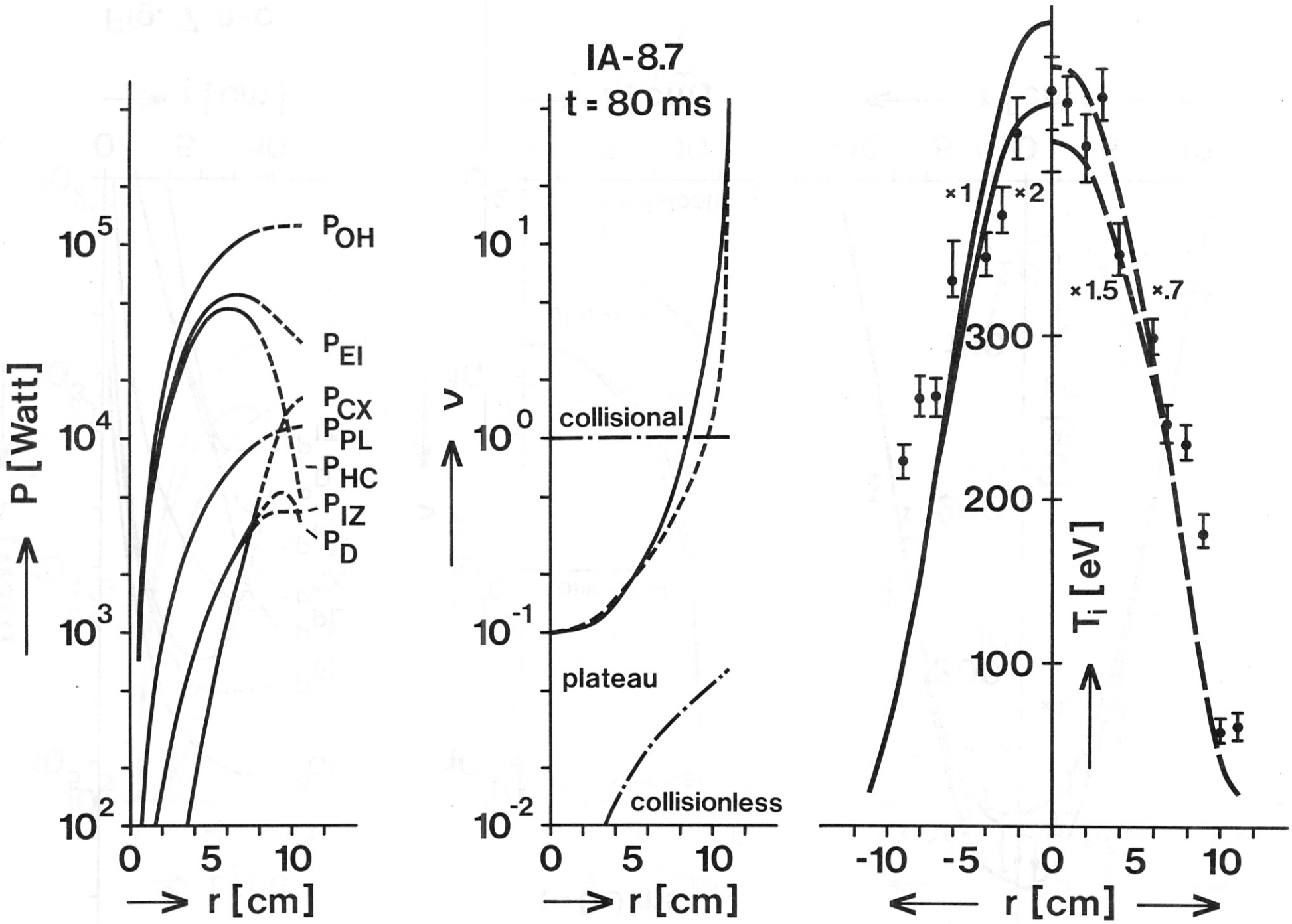
IA-8.7
t = 80 ms
P [Watt]
10^5
10^4
10^3
10^2
P_{OH}
P_{EI}
P_{CX}
P_{PL}
P_{HC}
P_{IZ}
P_D
0 5 10
r [cm]
ν
10^1
10^0
10^{-1}
10^{-2}
collisional
plateau
collisionless
0 5 10
r [cm]
×1
×2
×1.5
×.7
300
200
100
T_i [eV]
-10 -5 0 5 10
r [cm]

Fig. 8 a-c

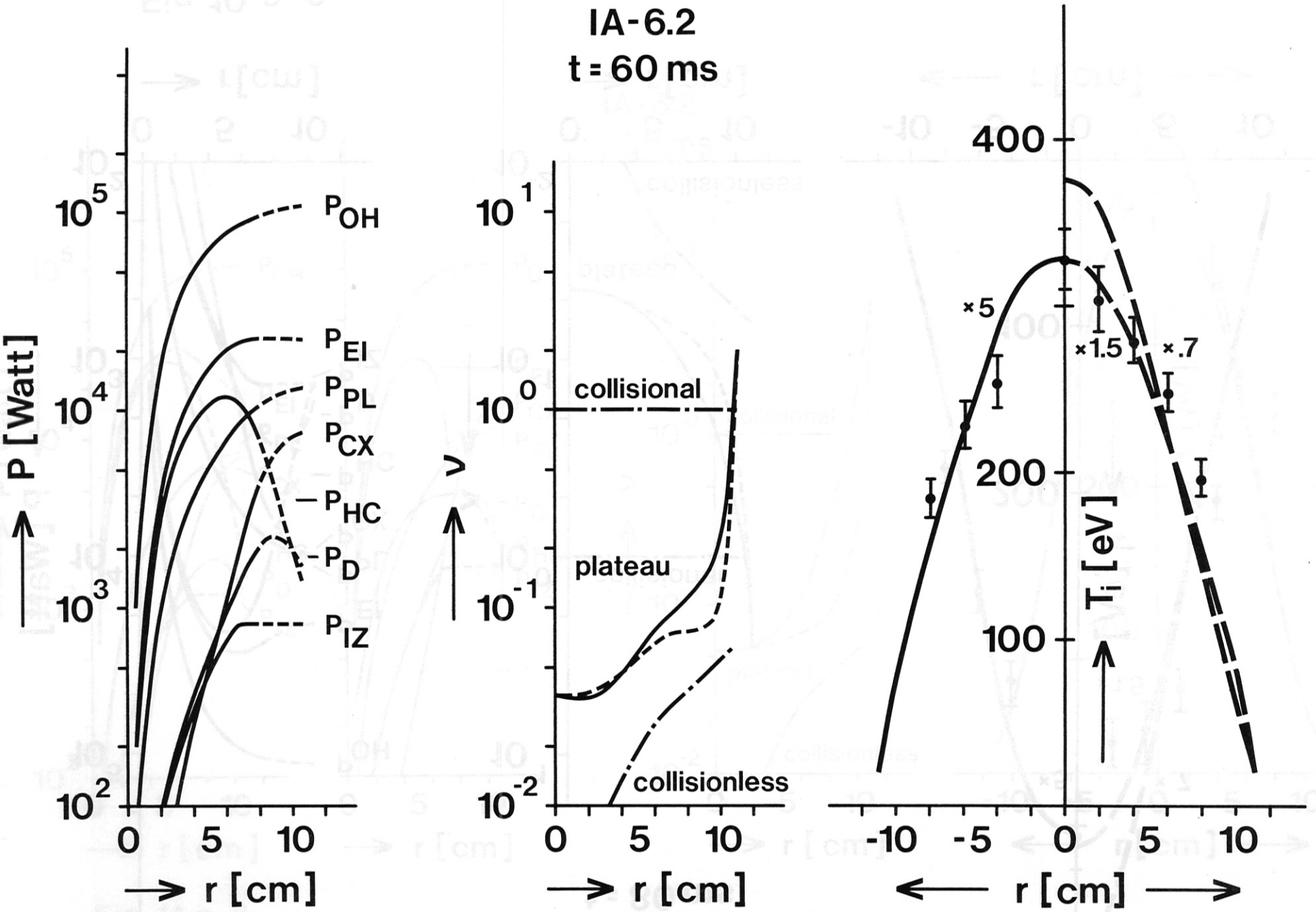
IA-6.2
t = 60 ms
P [Watt]
10^5
10^4
10^3
10^2
P_{OH}
P_{EI}
P_{PL}
P_{CX}
P_{HC}
P_D
P_{IZ}
0 5 10
r [cm]
ν
10^1
10^0
10^{-1}
10^{-2}
collisional
plateau
collisionless
0 5 10
r [cm]
400
200
100
T_i [eV]
×5
×1.5
×.7
-10 -5 0 5 10
r [cm]

Fig. 9 a-c

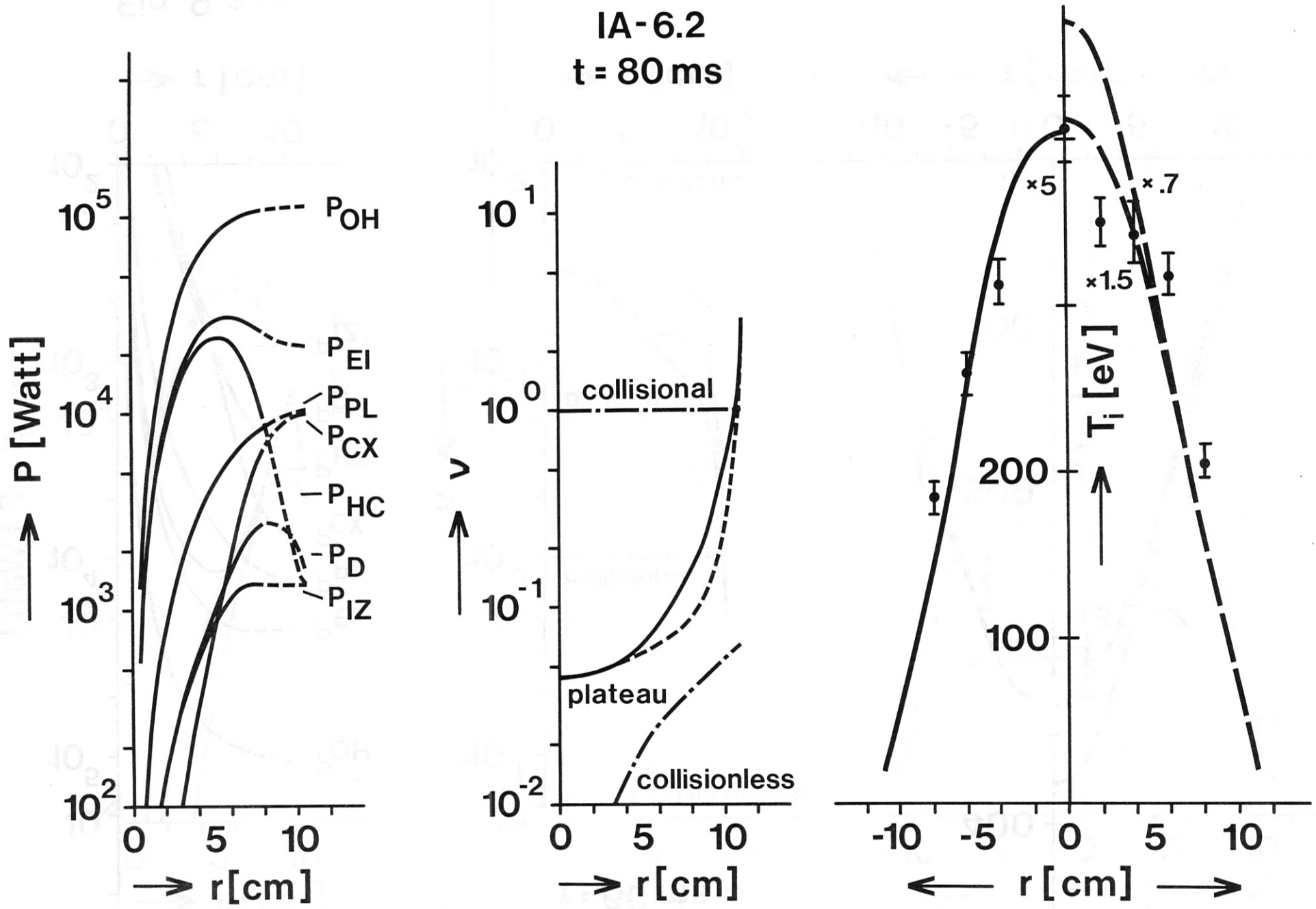
IA-6.2
t = 80 ms
P [Watt]
10^5
10^4
10^3
10^2
P_{OH}
P_{EI}
P_{PL}
P_{CX}
P_{HC}
P_D
P_{IZ}
0 5 10
r[cm]
ν
10^1
10^0
10^{-1}
10^{-2}
collisional
plateau
collisionless
0 5 10
r[cm]
×5
×1.5
×.7
T_i [eV]
200
100
-10 -5 0 5 10
r[cm]

Fig. 10 a-c

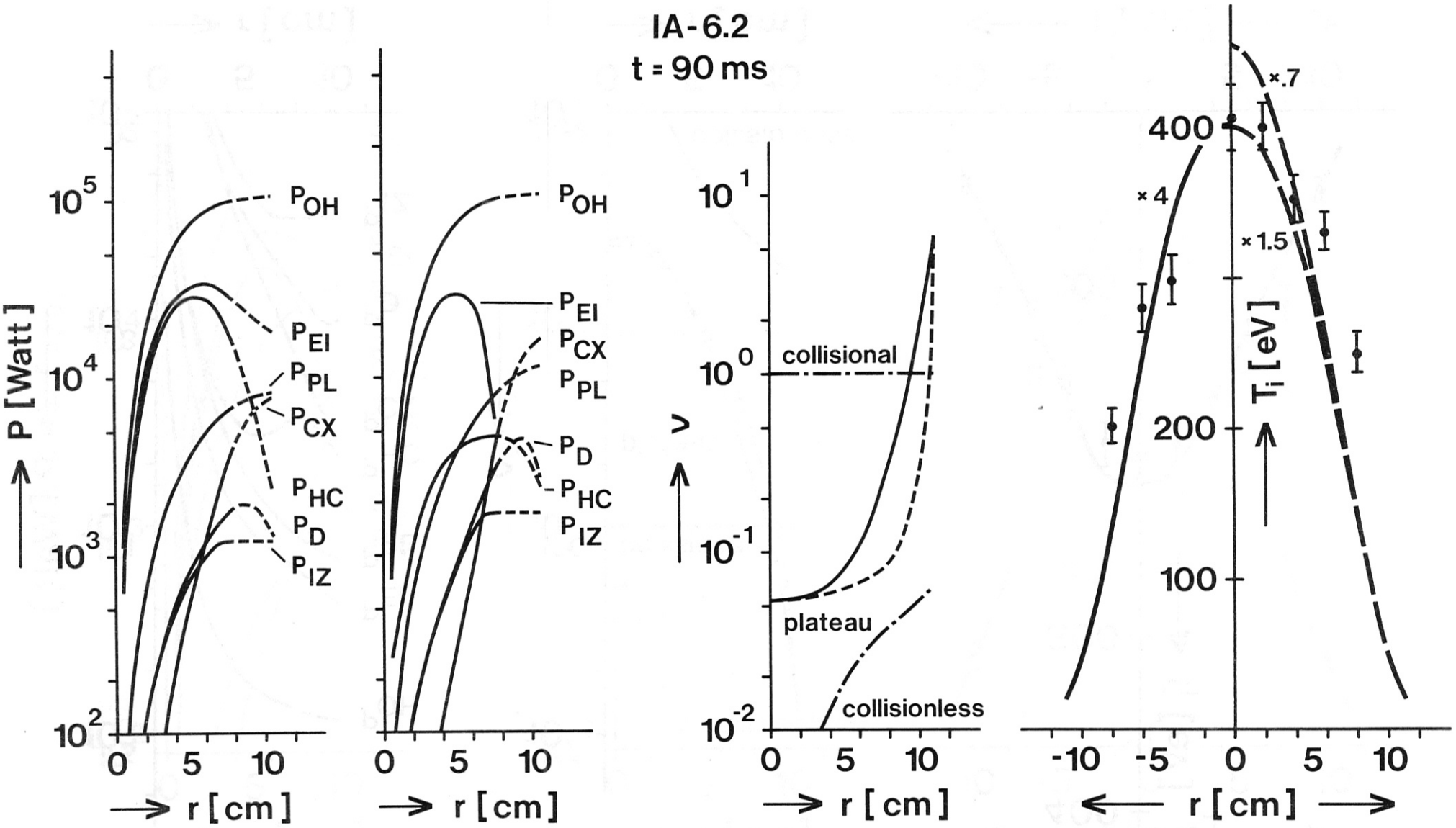
IA-6.2
t = 90 ms
P [Watt]
10^5
10^4
10^3
10^2
P_{OH}
P_{EI}
P_{PL}
P_{CX}
P_{HC}
P_D
P_{IZ}
0 5 10
r [cm]
P_{OH}
P_{EI}
P_{CX}
P_{PL}
P_D
P_{HC}
P_{IZ}
0 5 10
r [cm]
10^1
10^0
10^{-1}
10^{-2}
ν
collisional
plateau
collisionless
0 5 10
r [cm]
×.7
400
×4
×1.5
200
100
T_i [eV]
-10 -5 0 5 10
r [cm]

Fig. 11 a-d

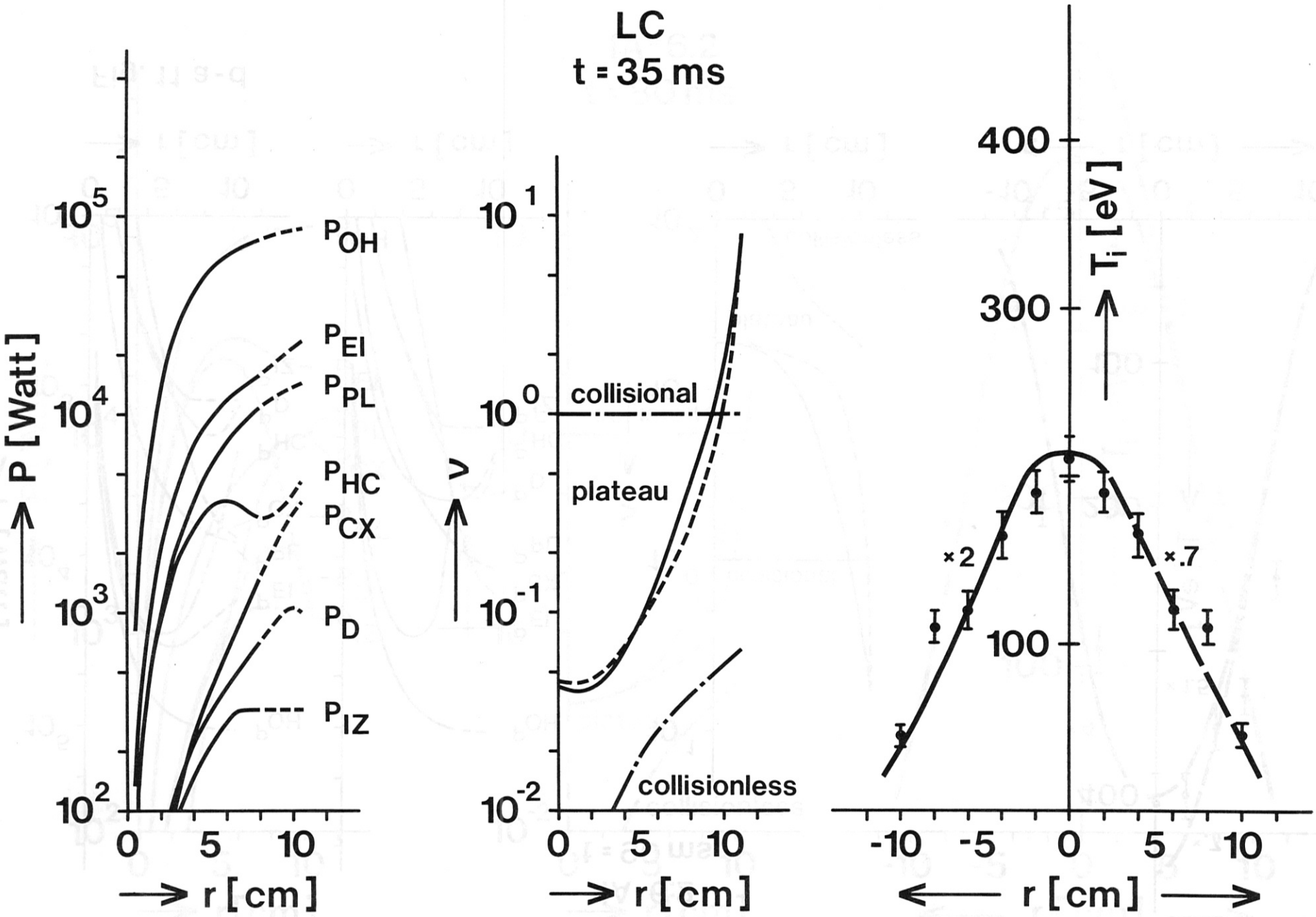
LC
t = 35 ms
P [Watt]
10^5
10^4
10^3
10^2
P_{OH}
P_{EI}
P_{PL}
P_{HC}
P_{CX}
P_D
P_{IZ}
0 5 10
r [cm]
ν
10^1
10^0
10^{-1}
10^{-2}
collisional
plateau
collisionless
0 5 10
r [cm]
T_i [eV]
400
300
100
×2
×.7
-10 -5 0 5 10
r [cm]

Fig. 12 a-c

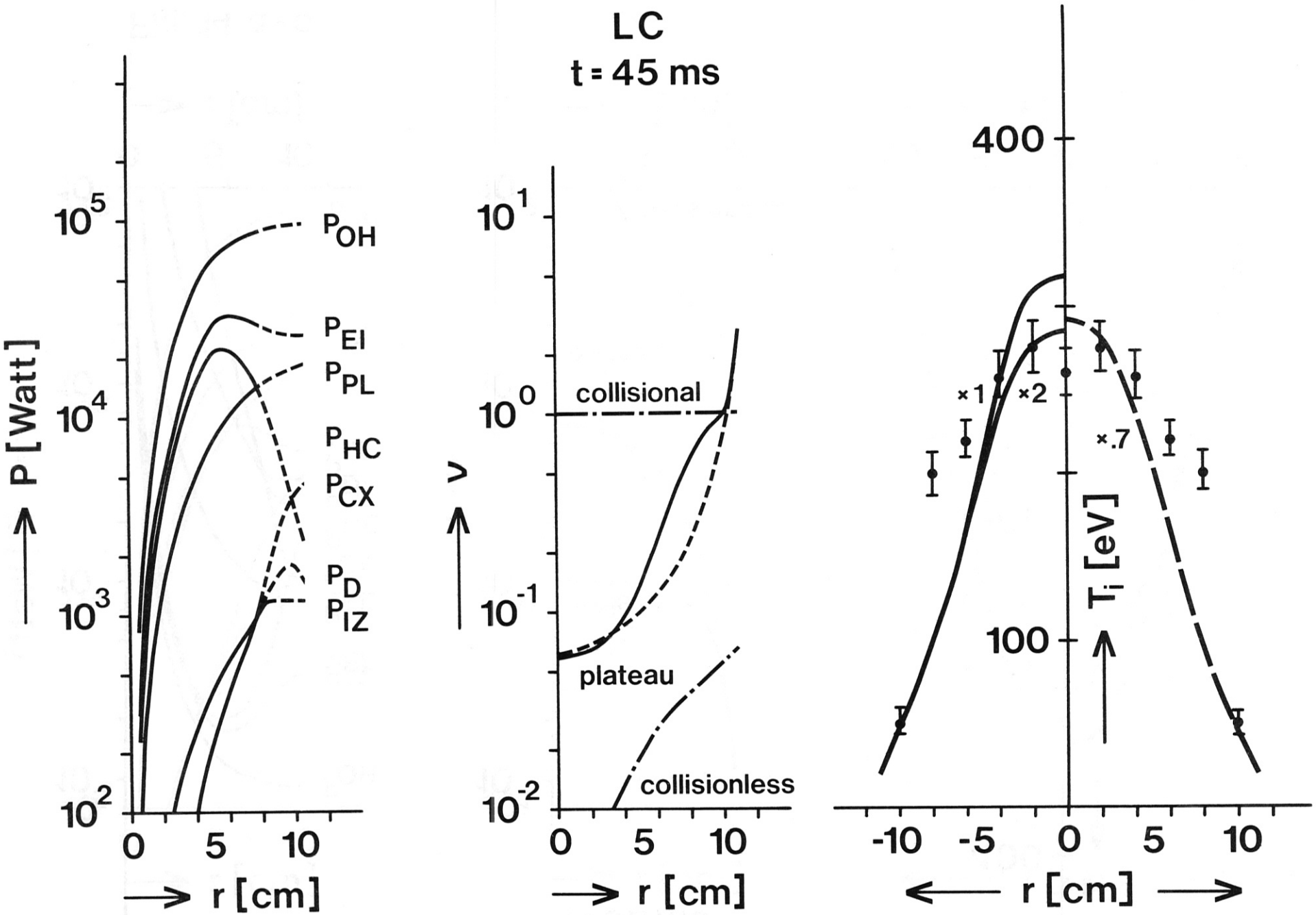
LC
t = 45 ms
P [Watt]
10^5
10^4
10^3
10^2
P_{OH}
P_{EI}
P_{PL}
P_{HC}
P_{CX}
P_D
P_{IZ}
0
5
10
r [cm]
ν
10^1
10^0
10^{-1}
10^{-2}
collisional
plateau
collisionless
0
5
10
r [cm]
400
100
T_i [eV]
×1
×2
×.7
-10
-5
0
5
10
r [cm]

Fig. 13 a-c

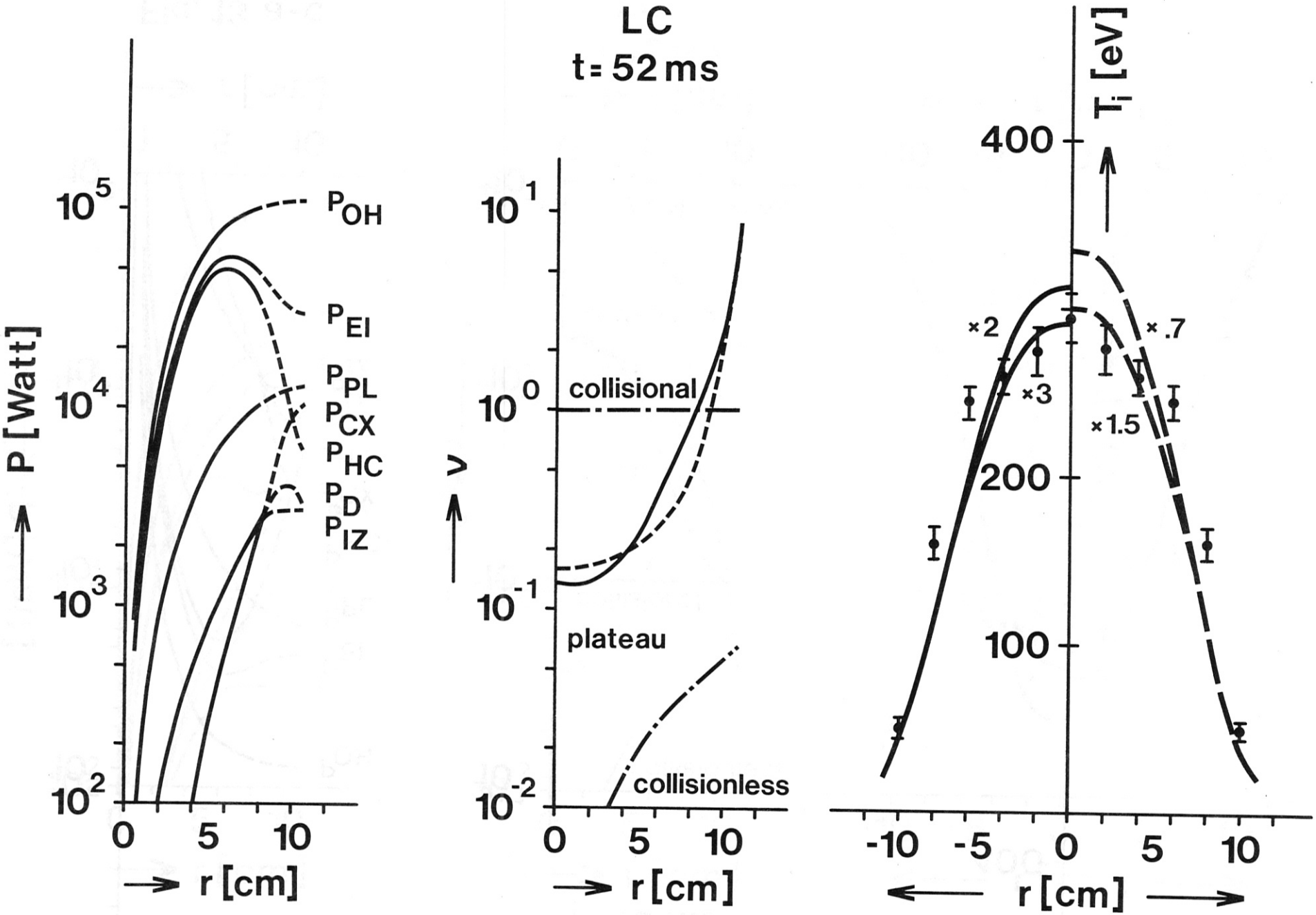
LC
t = 52 ms
P [Watt]
10^5
10^4
10^3
10^2
P_{OH}
P_{EI}
P_{PL}
P_{CX}
P_{HC}
P_D
P_{IZ}
0
5
10
r [cm]
ν
10^1
10^0
10^{-1}
10^{-2}
collisional
plateau
collisionless
0
5
10
r [cm]
T_i [eV]
400
200
100
×2
×3
×1.5
× .7
-10
-5
0
5
10
r [cm]

Fig. 14 a - c

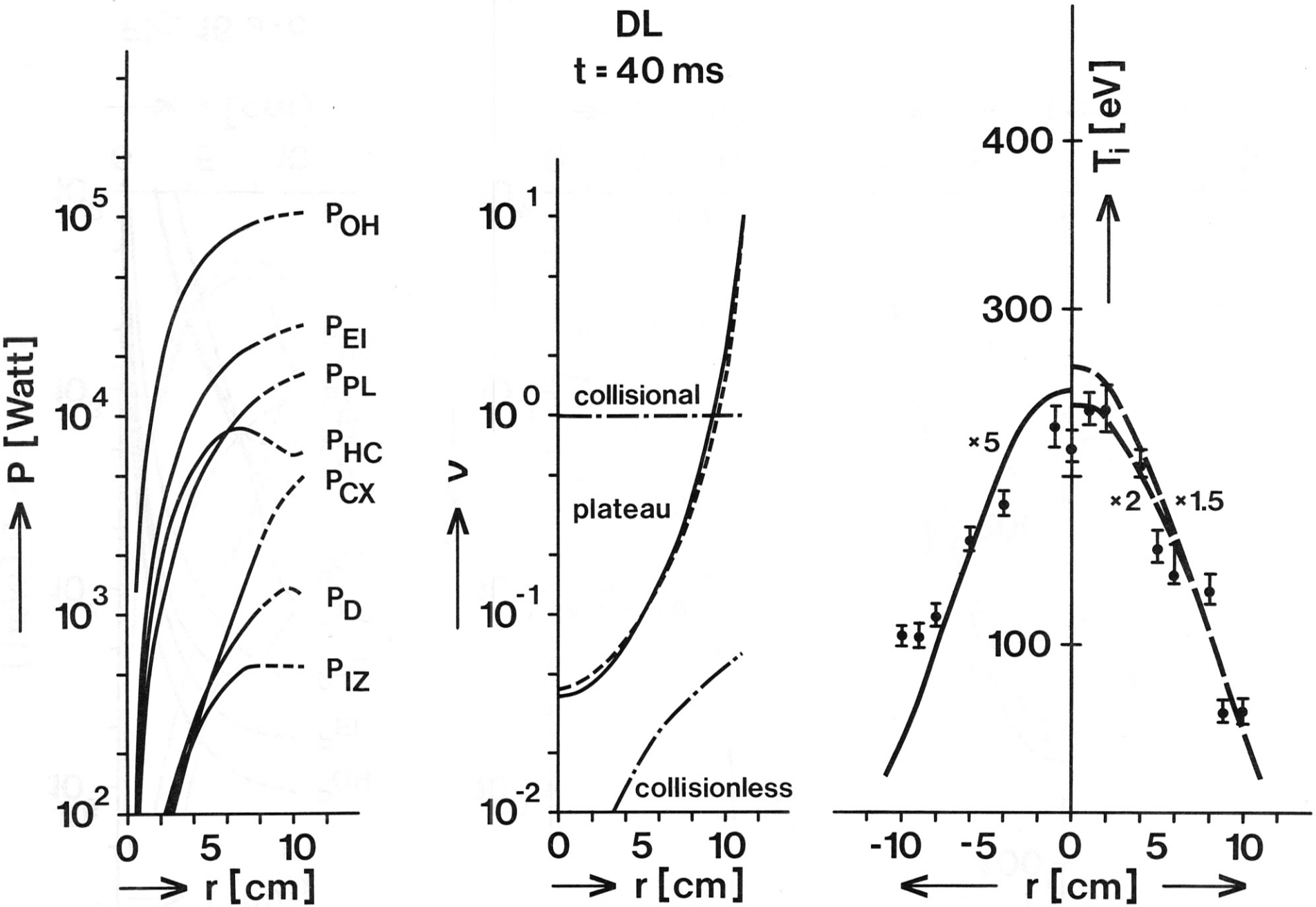
DL
t = 40 ms
P [Watt]
10^5
10^4
10^3
10^2
P_{OH}
P_{EI}
P_{PL}
P_{HC}
P_{CX}
P_D
P_{IZ}
0
5
10
r [cm]
ν
10^1
10^0
10^{-1}
10^{-2}
collisional
plateau
collisionless
0
5
10
r [cm]
T_i [eV]
400
300
100
×5
×2
×1.5
-10
-5
0
5
10
r [cm]

Fig. 15 a - c

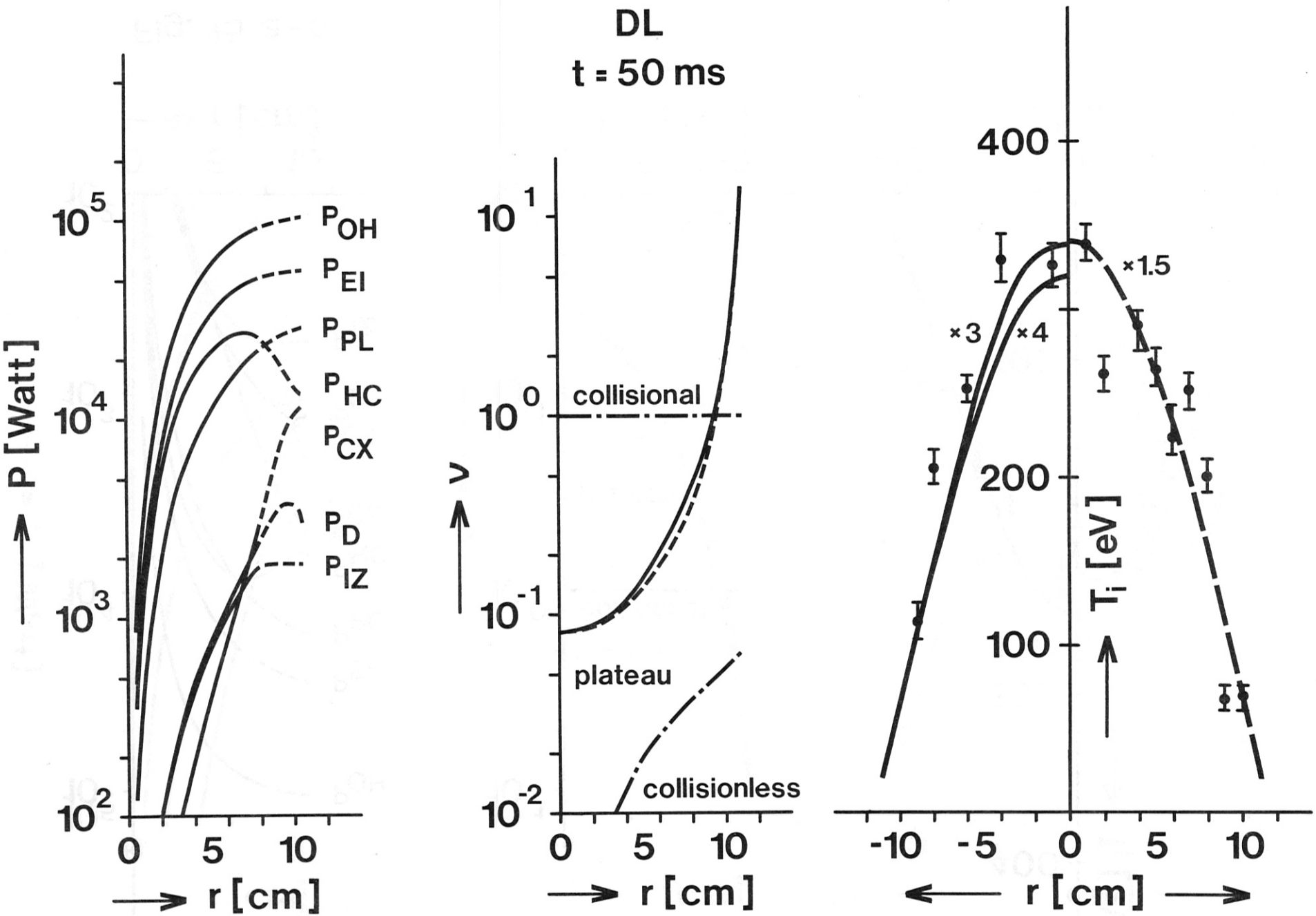
DL
t = 50 ms
P [Watt]
10^5
10^4
10^3
10^2
P_{OH}
P_{EI}
P_{PL}
P_{HC}
P_{CX}
P_D
P_{IZ}
0 5 10
r [cm]
ν
10^1
10^0
10^{-1}
10^{-2}
collisional
plateau
collisionless
0 5 10
r [cm]
400
200
100
T_i [eV]
×3
×4
×1.5
-10 -5 0 5 10
r [cm]

Fig. 16 a-c

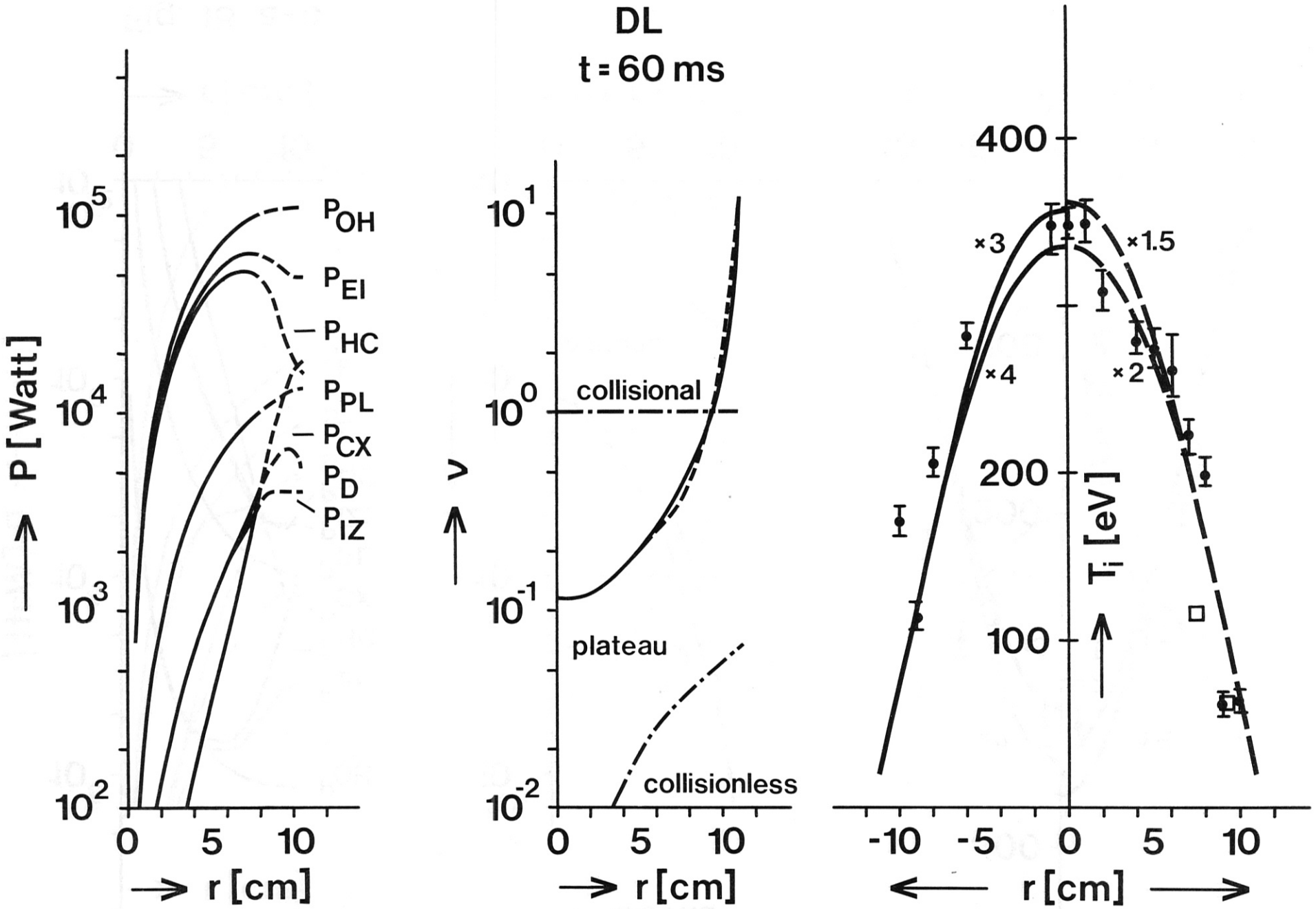
DL
t = 60 ms
P [Watt]
10^5
10^4
10^3
10^2
P_{OH}
P_{EI}
P_{HC}
P_{PL}
P_{CX}
P_D
P_{IZ}
0 5 10
r [cm]
ν
10^1
10^0
10^{-1}
10^{-2}
collisional
plateau
collisionless
0 5 10
r [cm]
400
200
100
T_i [eV]
×3
×4
×1.5
×2
-10 -5 0 5 10
r [cm]

Fig. 17 a-c

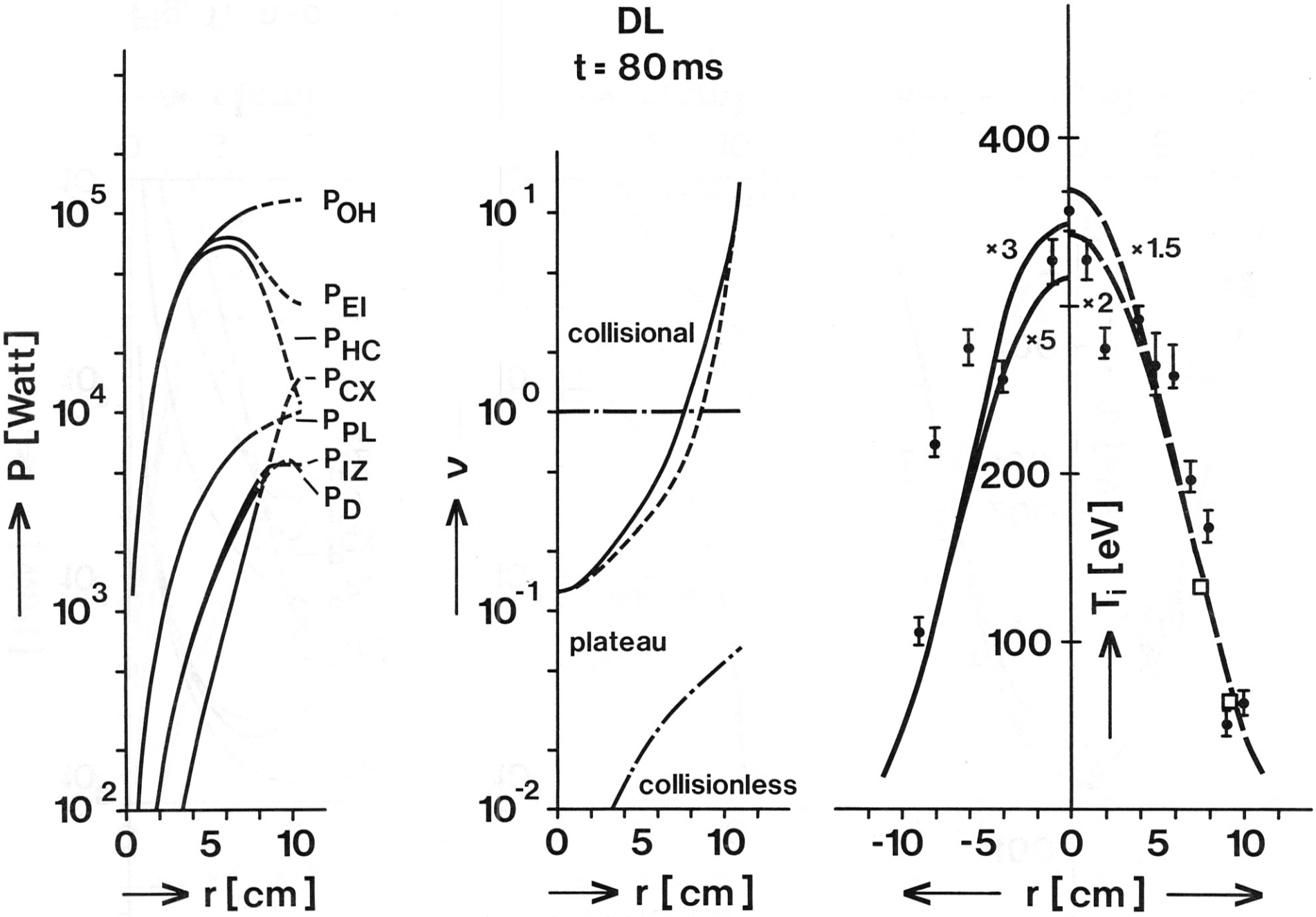
DL
t = 80 ms
P [Watt]
10^5
10^4
10^3
10^2
P_{OH}
P_{EI}
P_{HC}
P_{CX}
P_{PL}
P_{IZ}
P_D
0
5
10
r [cm]
ν
10^1
10^0
10^{-1}
10^{-2}
collisional
plateau
collisionless
0
5
10
r [cm]
400
200
100
T_i [eV]
×3
×1.5
×2
×5
-10
-5
0
5
10
r [cm]

Fig. 18 a-c

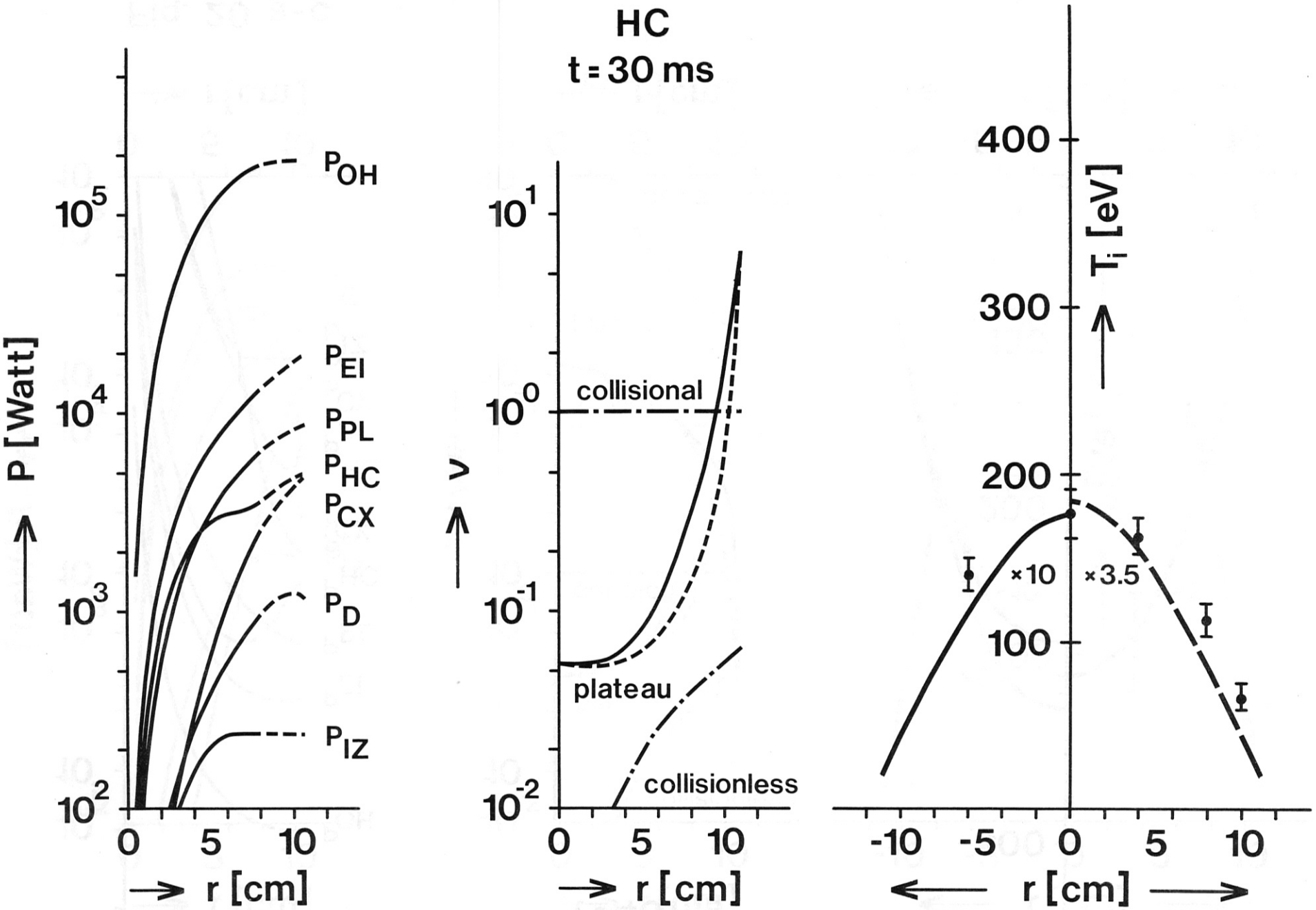
HC
t = 30 ms
P [Watt]
10^5
10^4
10^3
10^2
P_{OH}
P_{EI}
P_{PL}
P_{HC}
P_{CX}
P_D
P_{IZ}
0 5 10
r [cm]
ν
10^1
10^0
10^{-1}
10^{-2}
collisional
plateau
collisionless
0 5 10
r [cm]
400
300
200
100
T_i [eV]
×10
×3.5
-10 -5 0 5 10
r [cm]

Fig. 19 a-c

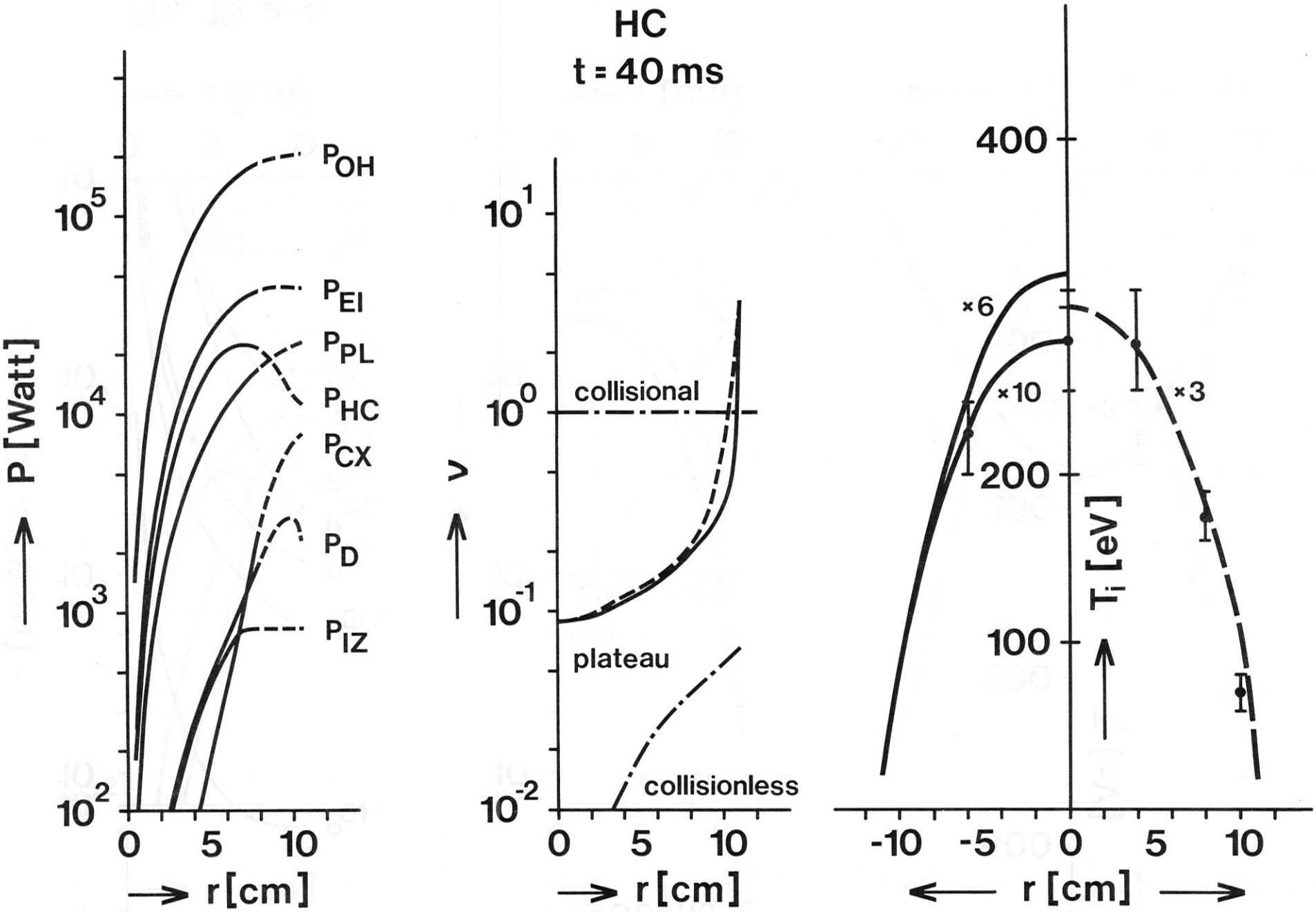
HC
t = 40 ms
P [Watt]
10^5
10^4
10^3
10^2
P_{OH}
P_{EI}
P_{PL}
P_{HC}
P_{CX}
P_D
P_{IZ}
0 5 10
r [cm]
ν
10^1
10^0
10^{-1}
10^{-2}
collisional
plateau
collisionless
0 5 10
r [cm]
400
200
100
×6
×10
×3
T_i [eV]
-10 -5 0 5 10
r [cm]

Fig. 20 a-c

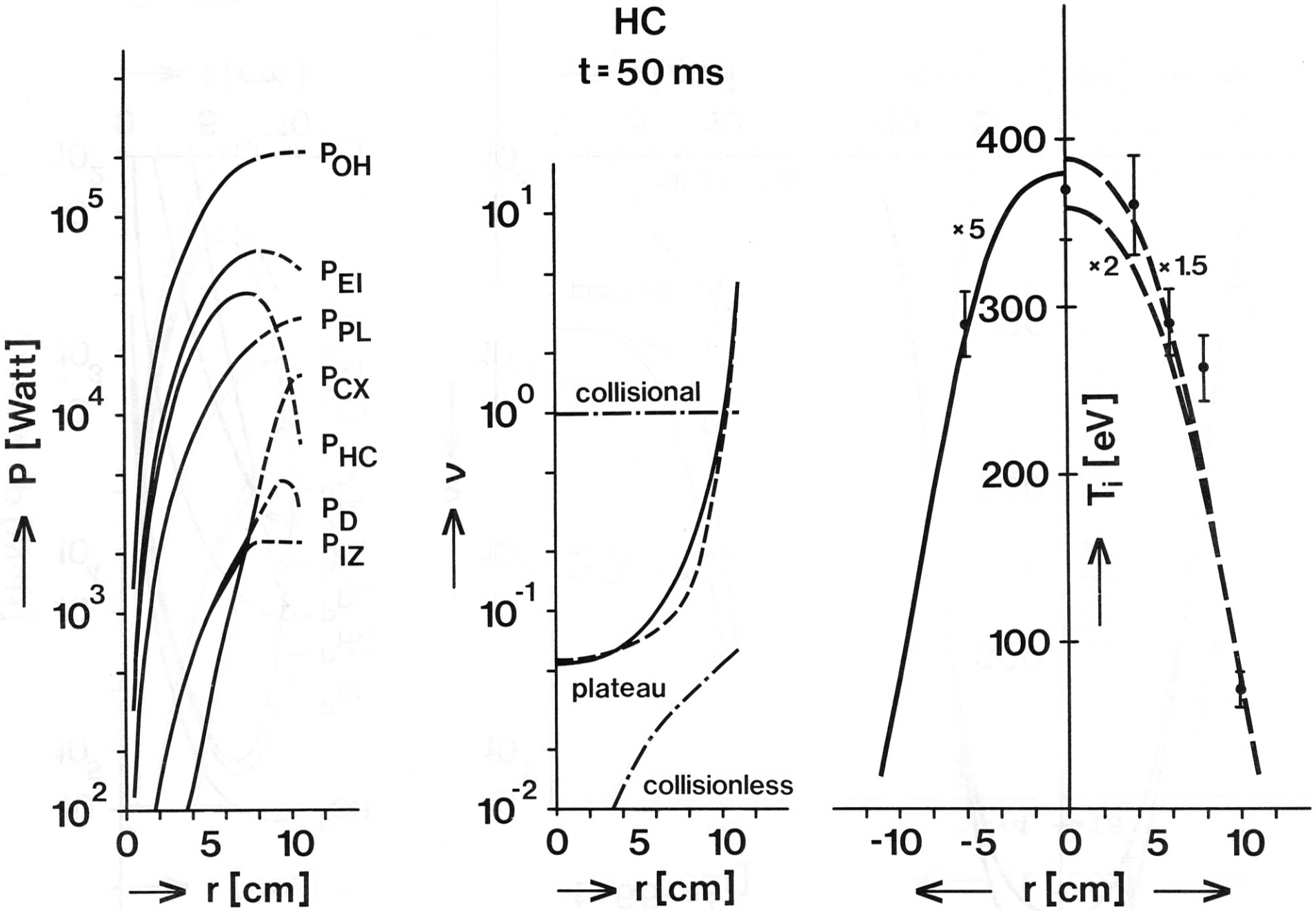
HC
t = 50 ms
P [Watt]
10^5
10^4
10^3
10^2
P_{OH}
P_{EI}
P_{PL}
P_{CX}
P_{HC}
P_D
P_{IZ}
0 5 10
r [cm]
ν
10^1
10^0
10^{-1}
10^{-2}
collisional
plateau
collisionless
0 5 10
r [cm]
400
300
200
100
T_i [eV]
×5
×2
×1.5
-10 -5 0 5 10
r [cm]

Fig. 21 a-c

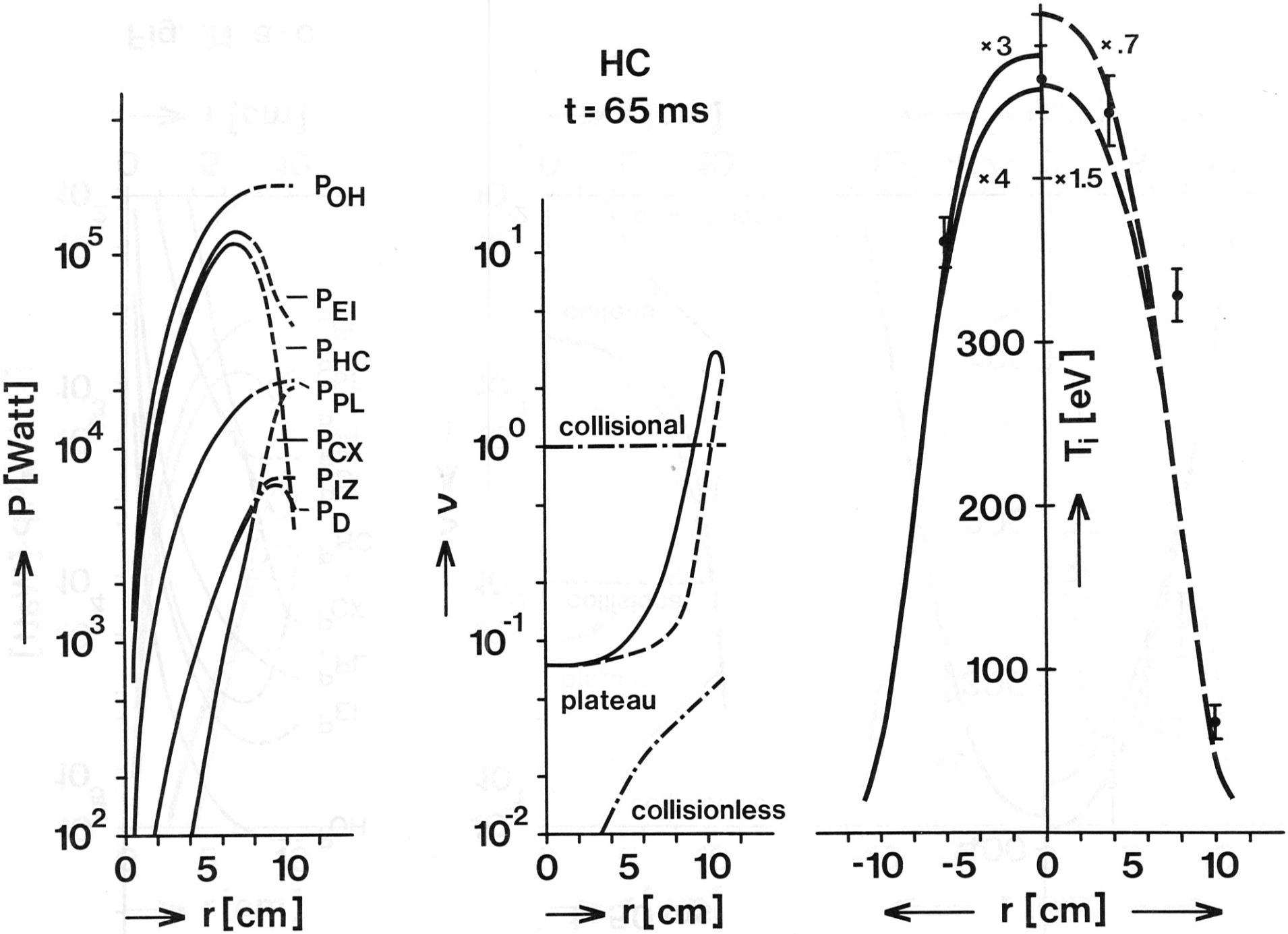
HC
t = 65 ms
P [Watt]
10^5
10^4
10^3
10^2
P_{OH}
P_{EI}
P_{HC}
P_{PL}
P_{CX}
P_{IZ}
P_D
0 5 10
r [cm]
ν
10^1
10^0
10^{-1}
10^{-2}
collisional
plateau
collisionless
0 5 10
r [cm]
×3
×.7
×4
×1.5
300
200
100
T_i [eV]
-10 -5 0 5 10
r [cm]

Fig. 22 a-c

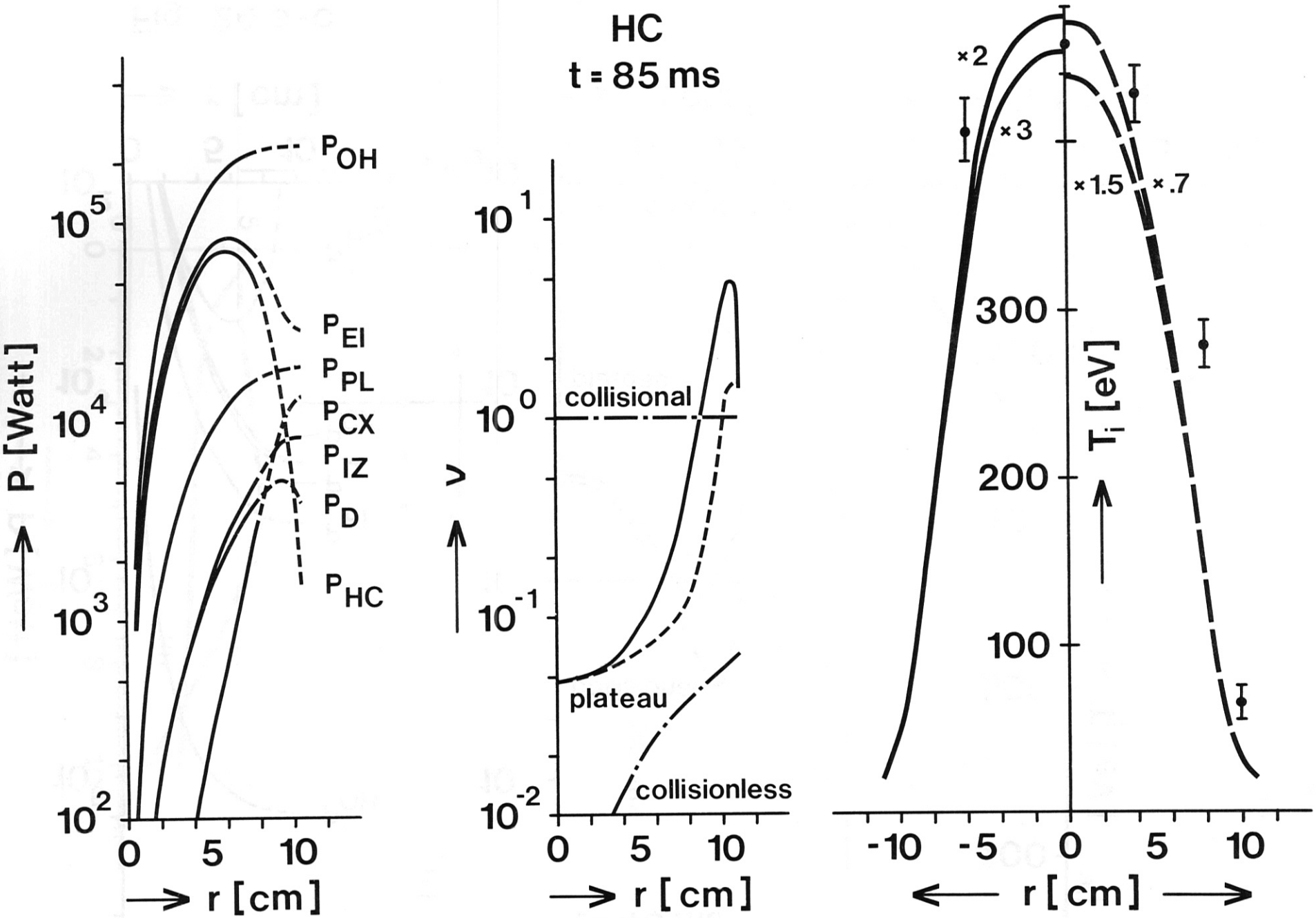
HC
t = 85 ms
P [Watt]
10^5
10^4
10^3
10^2
P_{OH}
P_{EI}
P_{PL}
P_{CX}
P_{IZ}
P_D
P_{HC}
0 5 10
r [cm]
ν
10^1
10^0
10^{-1}
10^{-2}
collisional
plateau
collisionless
0 5 10
r [cm]
×2
×3
×1.5
×.7
300
200
100
T_i [eV]
-10 -5 0 5 10
r [cm]

Fig. 23 a-c

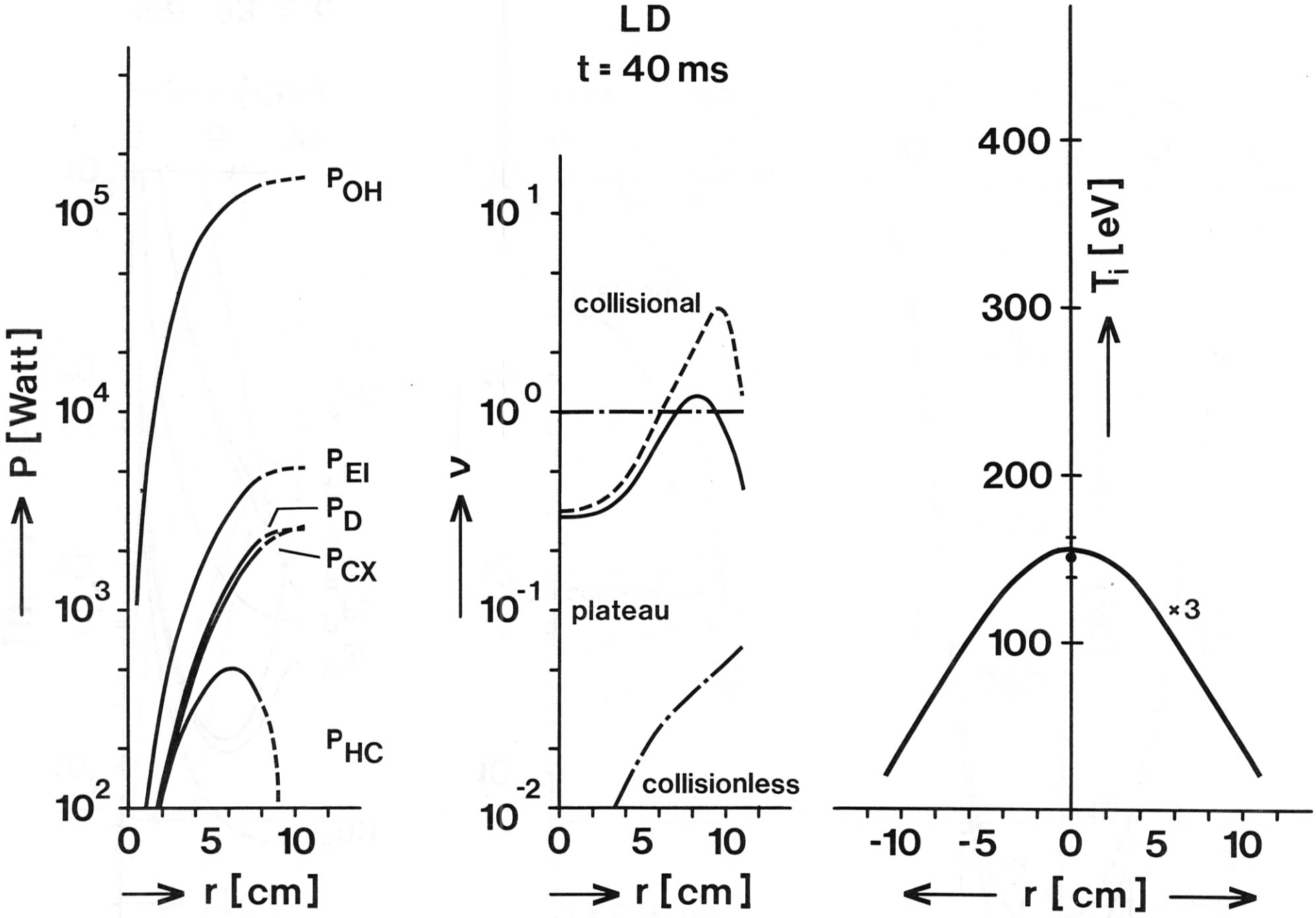
LD
t = 40 ms
P [Watt]
10^5
10^4
10^3
10^2
P_{OH}
P_{EI}
P_D
P_{CX}
P_{HC}
0 5 10
r [cm]
ν
10^1
10^0
10^{-1}
10^{-2}
collisional
plateau
collisionless
0 5 10
r [cm]
T_i [eV]
400
300
200
100
×3
-10 -5 0 5 10
r [cm]

Fig. 24 a-c

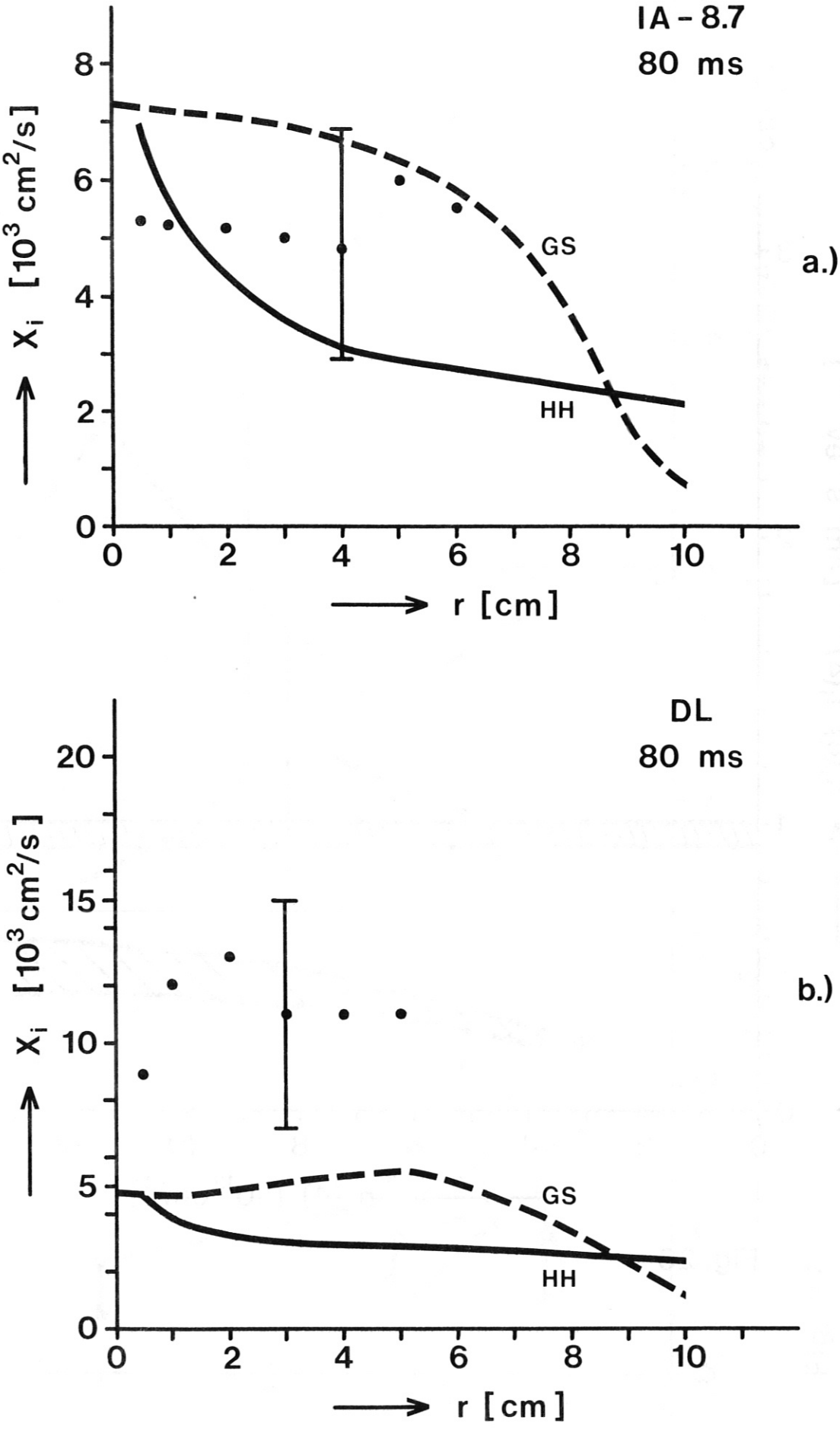

Fig. 25

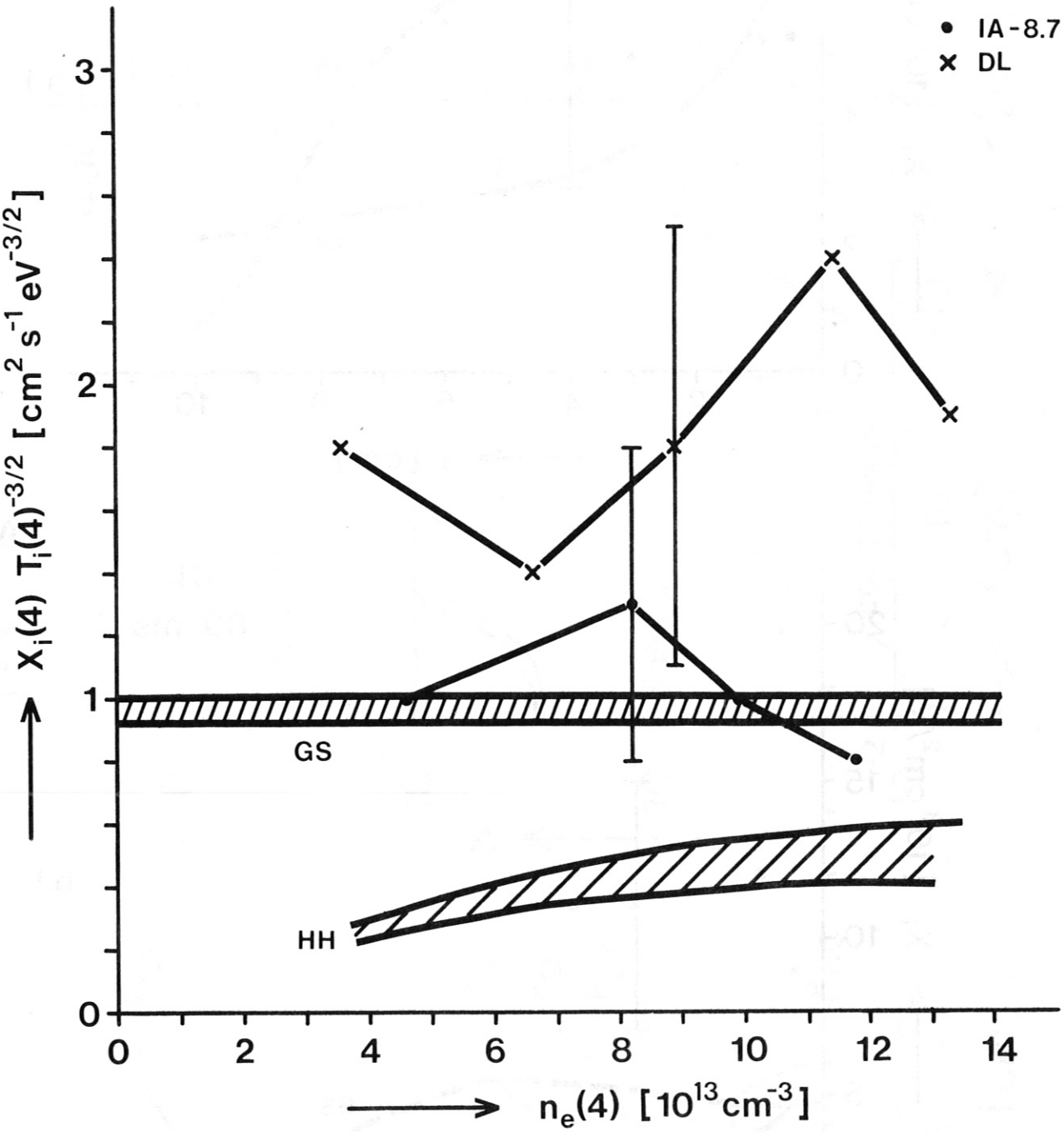
• IA-8.7
× DL
3
2
1
0
GS
HH
0
2
4
6
8
10
12
14
$X_i(4)\ T_i(4)^{-3/2}\ [cm^2\ s^{-1}\ eV^{-3/2}]$
$n_e(4)\ [10^{13} cm^{-3}]$

Fig. 26

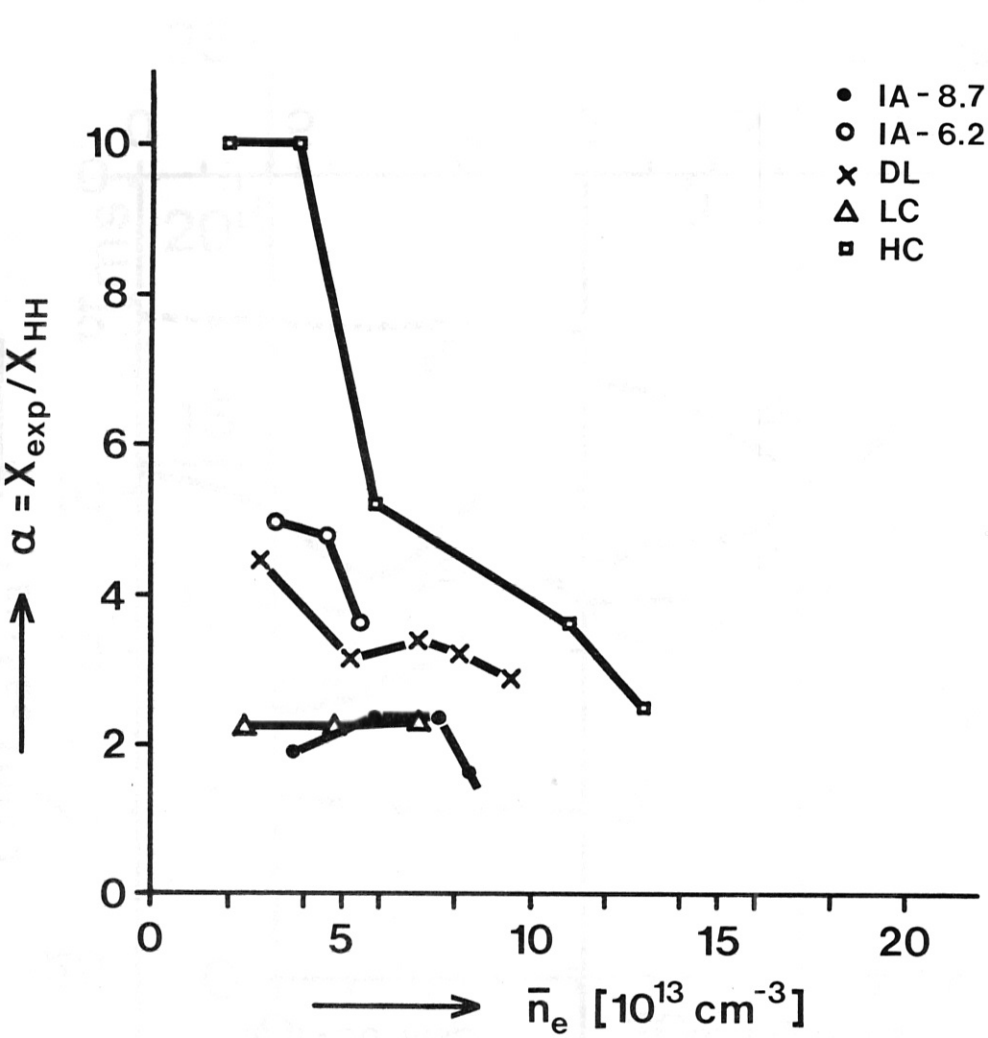
• IA - 8.7
o IA - 6.2
× DL
△ LC
▫ HC
α = X_exp / X_HH
0
2
4
6
8
10
0
5
10
15
20
n̄_e [10^13 cm^-3]

a.)

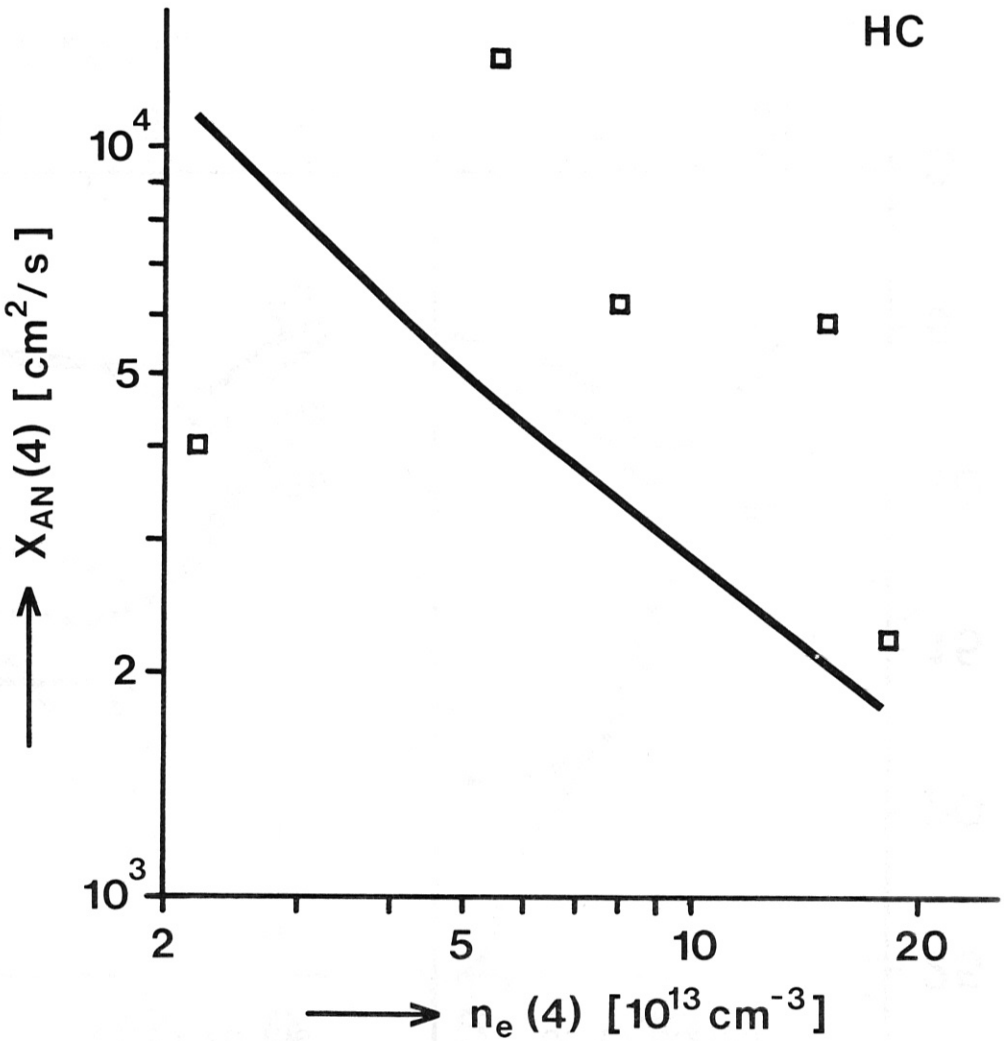
HC
X_AN(4) [cm^2/s]
10^3
2
5
10^4
2
5
10
20
n_e (4) [10^13 cm^-3]

b.)

Fig. 27

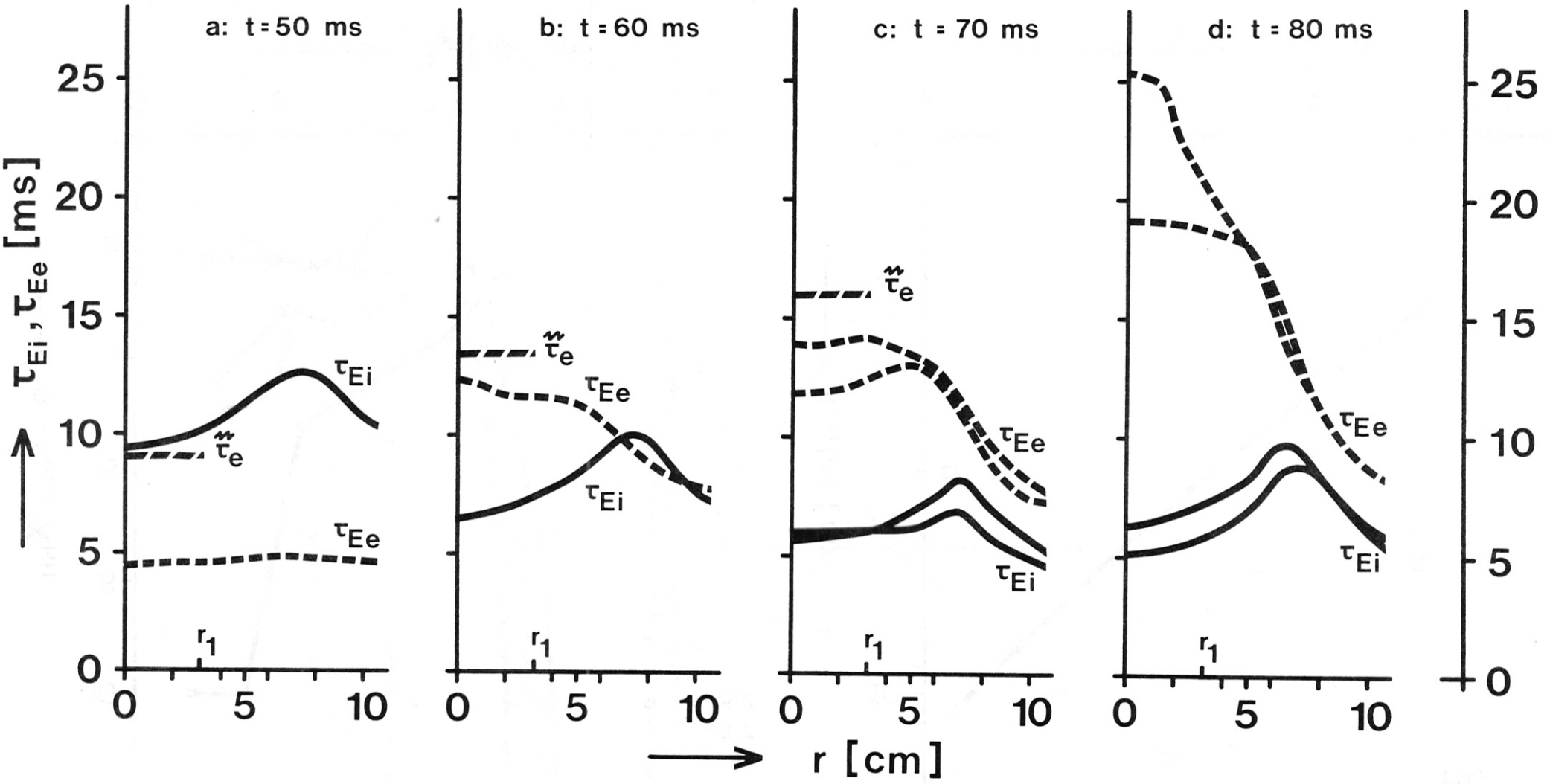
a: t = 50 ms
b: t = 60 ms
c: t = 70 ms
d: t = 80 ms
τ_{Ei}, τ_{Ee} [ms]
τ_{Ei}
τ_{Ee}
$\tilde{\tau}_e$
r_1
0
5
10
15
20
25
r [cm]

Fig. 28 a-d

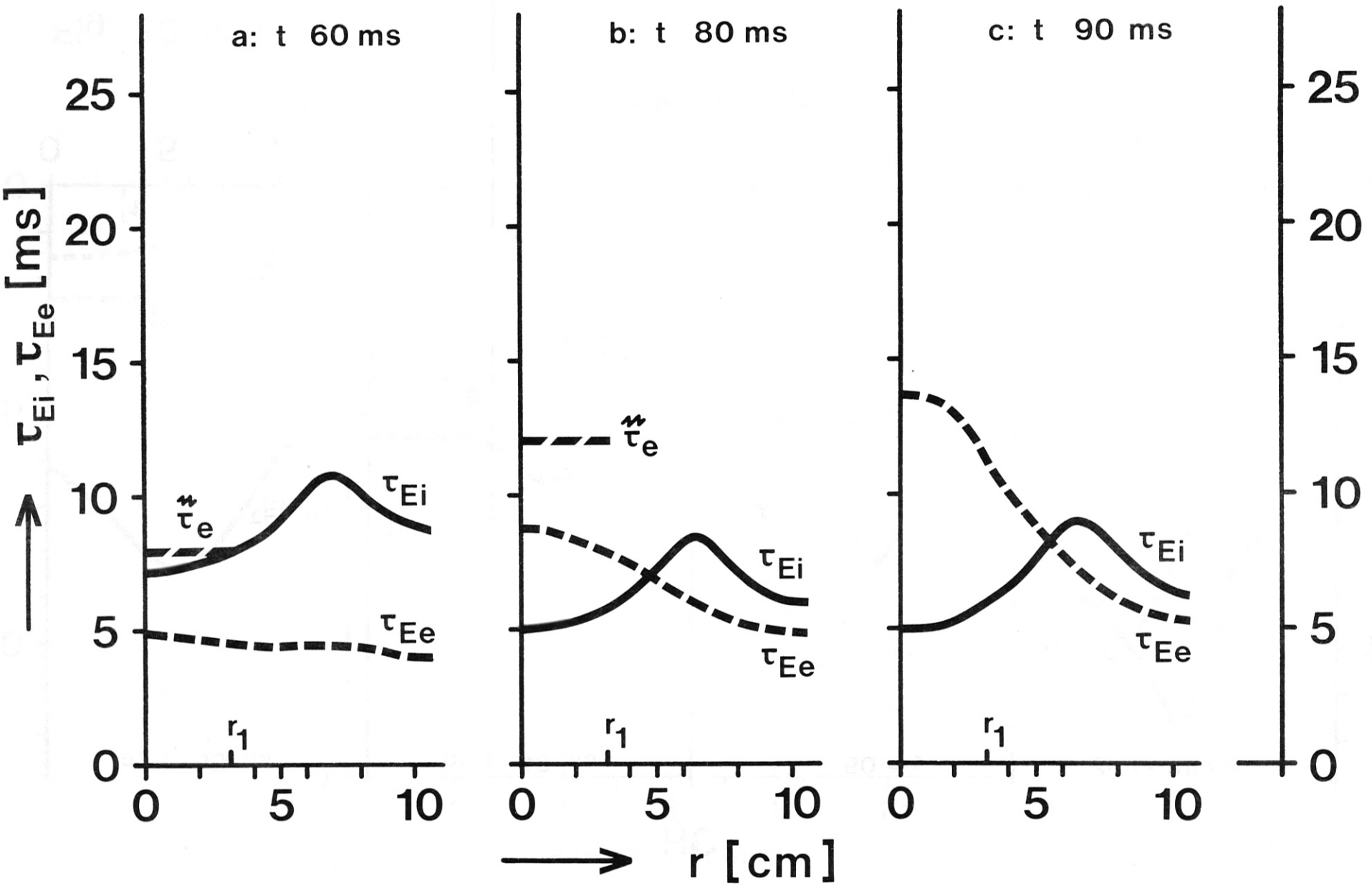
a: t 60 ms
b: t 80 ms
c: t 90 ms
τ_{Ei}, τ_{Ee} [ms]
τ_e^*
τ_{Ei}
τ_{Ee}
r_1
0
5
10
15
20
25
r [cm]

Fig. 29 a-c

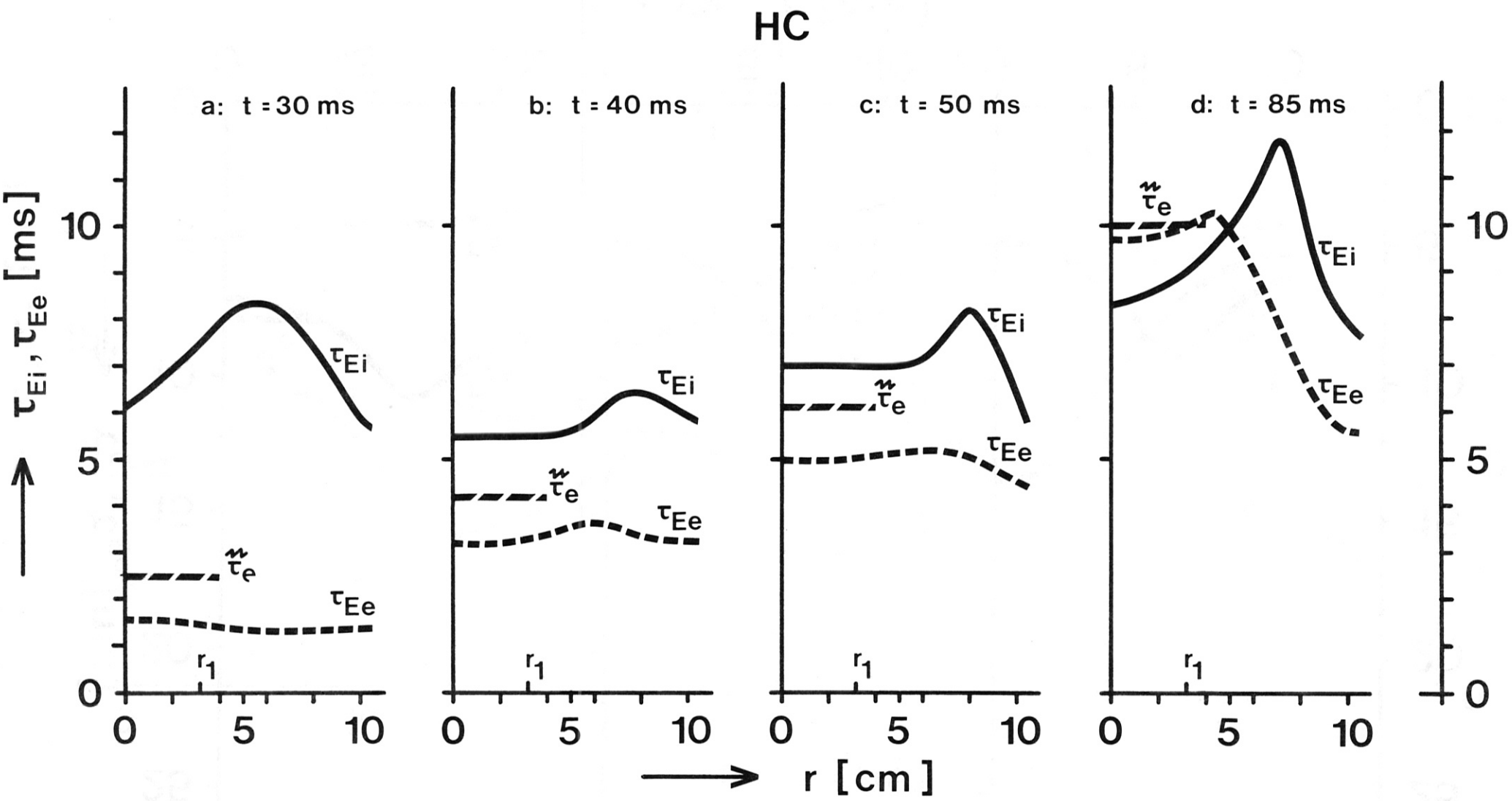
HC
a: t = 30 ms
b: t = 40 ms
c: t = 50 ms
d: t = 85 ms
τ_{Ei} , τ_{Ee} [ms]
τ_{Ei}
$\tilde{\tau}_e$
τ_{Ee}
r_1
0
5
10
r [cm]

Fig. 30 a-d

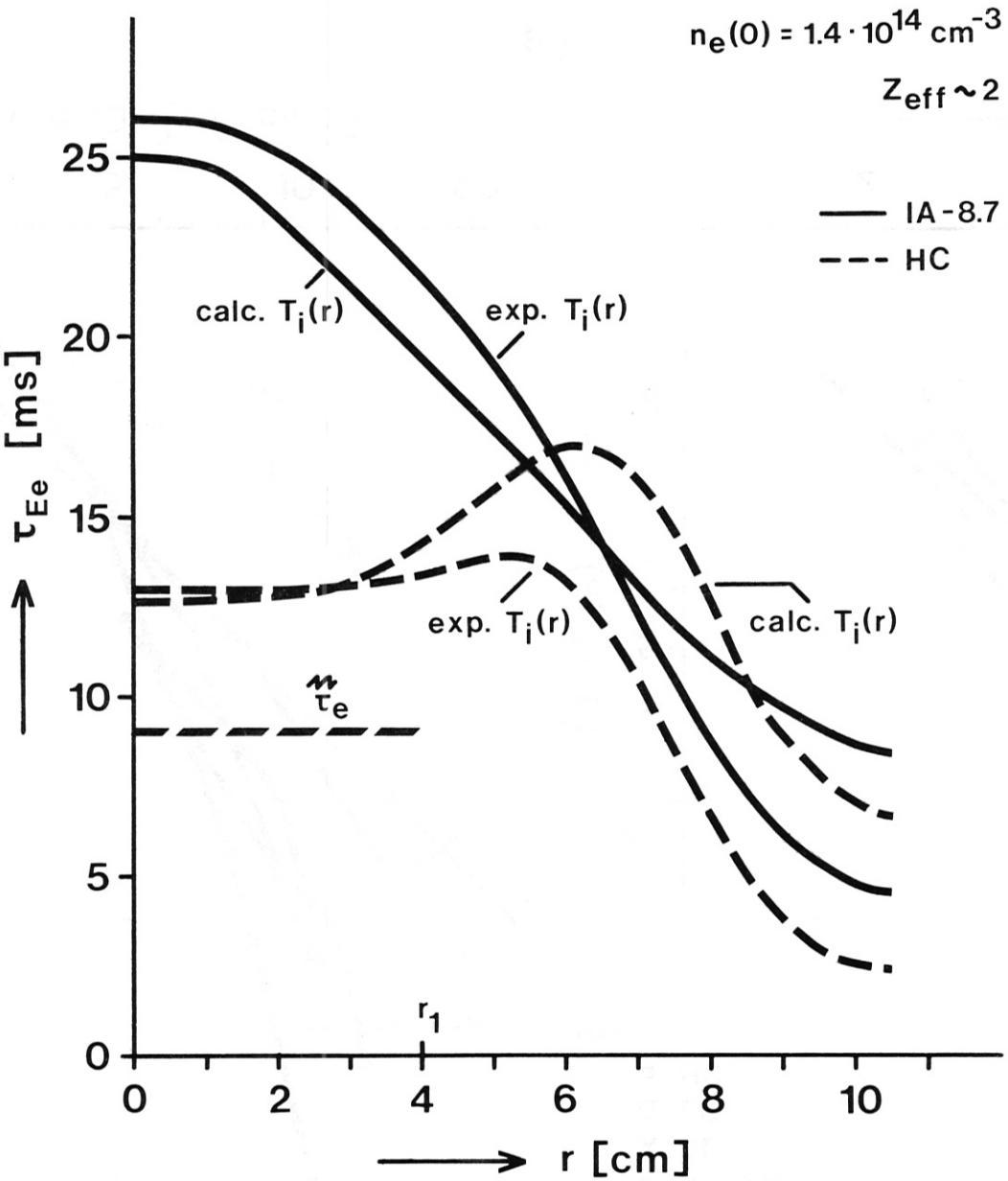
$n_e(0) = 1.4 \cdot 10^{14}\ cm^{-3}$
$Z_{eff} \sim 2$
IA-8.7
HC
calc. $T_i(r)$
exp. $T_i(r)$
exp. $T_i(r)$
calc. $T_i(r)$
τ_e
τ_{Ee} [ms]
r_1
r [cm]
0
5
10
15
20
25
0
2
4
6
8
10

Fig. 31

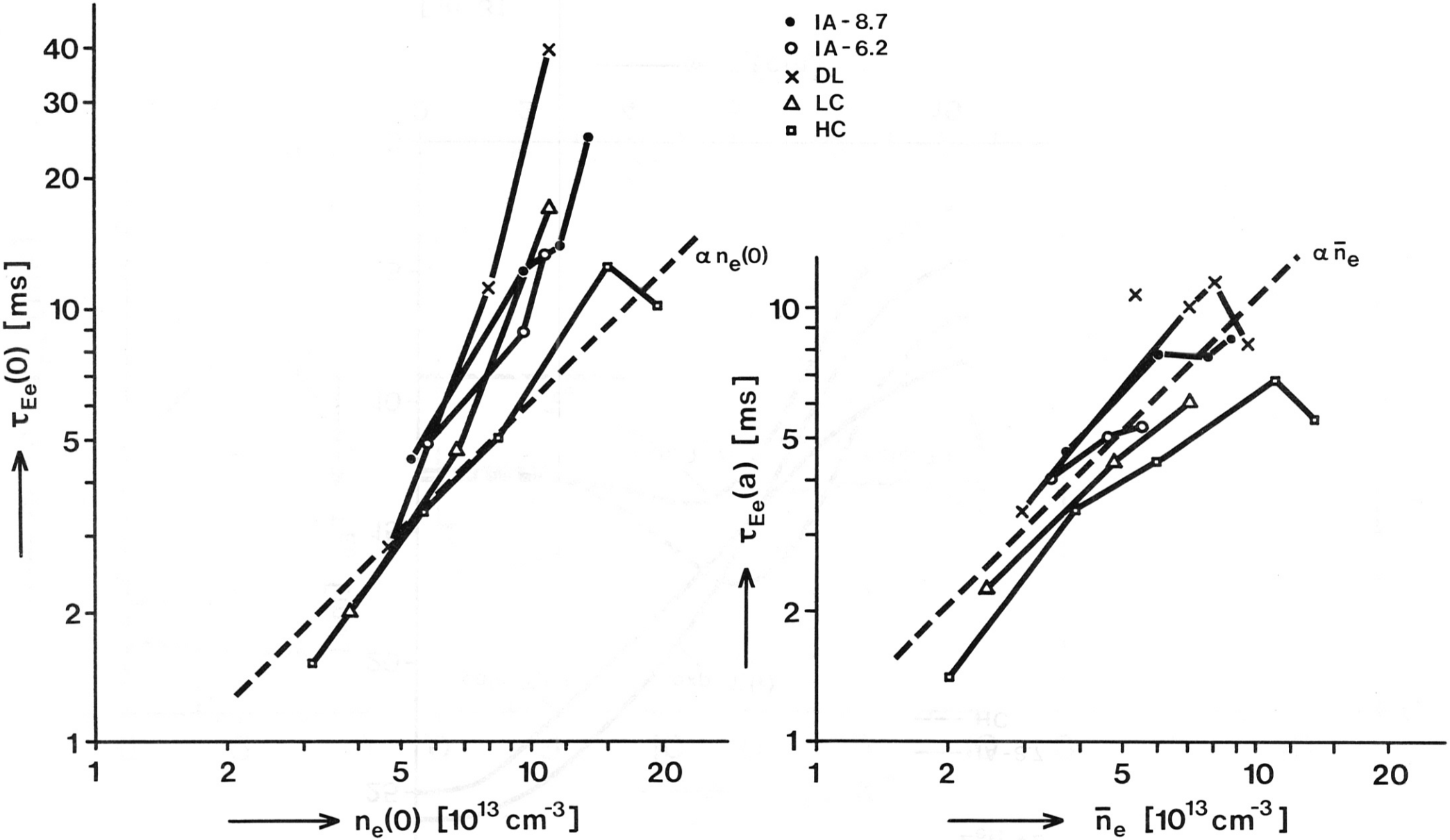
IA - 8.7
IA - 6.2
DL
LC
HC
$\alpha\, n_e(0)$
$\alpha\, \bar{n}_e$
$\tau_{Ee}(0)$ [ms]
$\tau_{Ee}(a)$ [ms]
$n_e(0)$ [10^{13} cm^{-3}]
$\bar{n}_e$ [10^{13} cm^{-3}]
40
30
20
10
5
2
1
1
2
5
10
20

Fig. 32

a.)

b.)

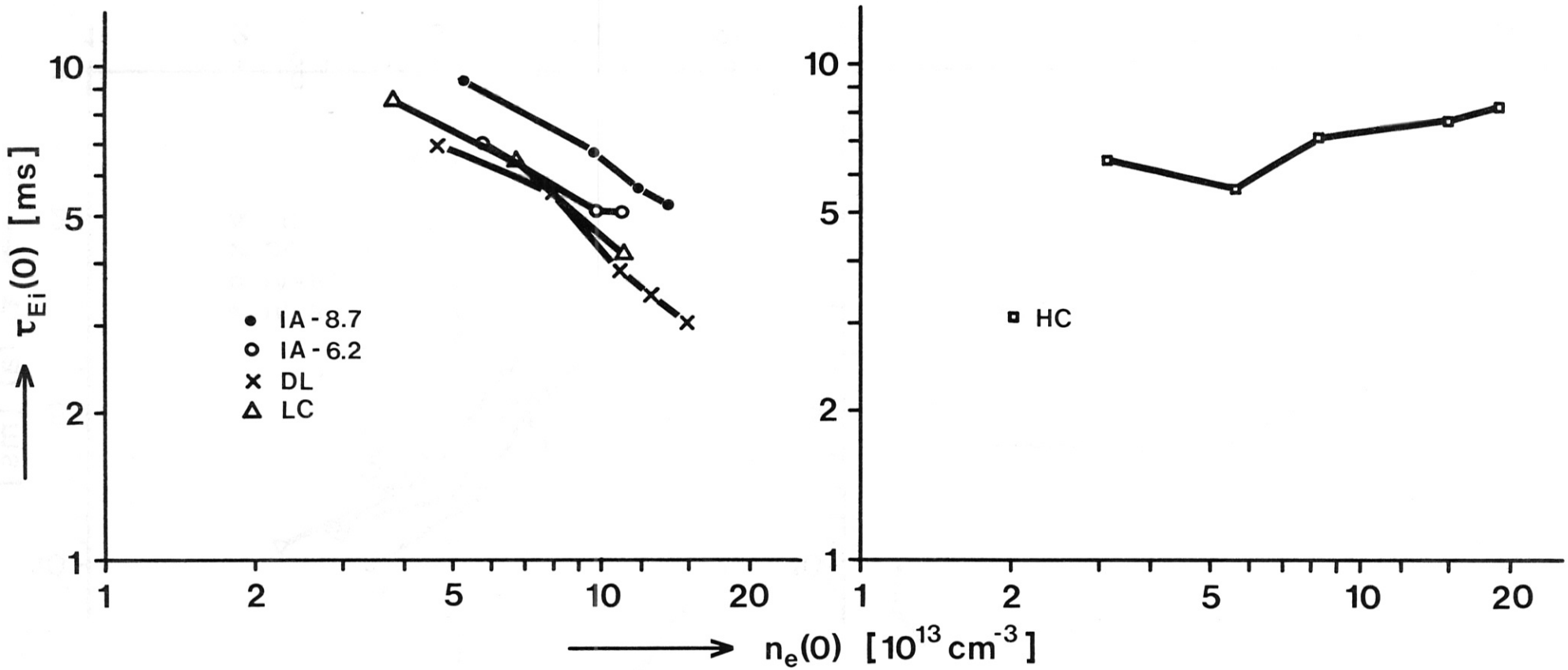

Fig. 33

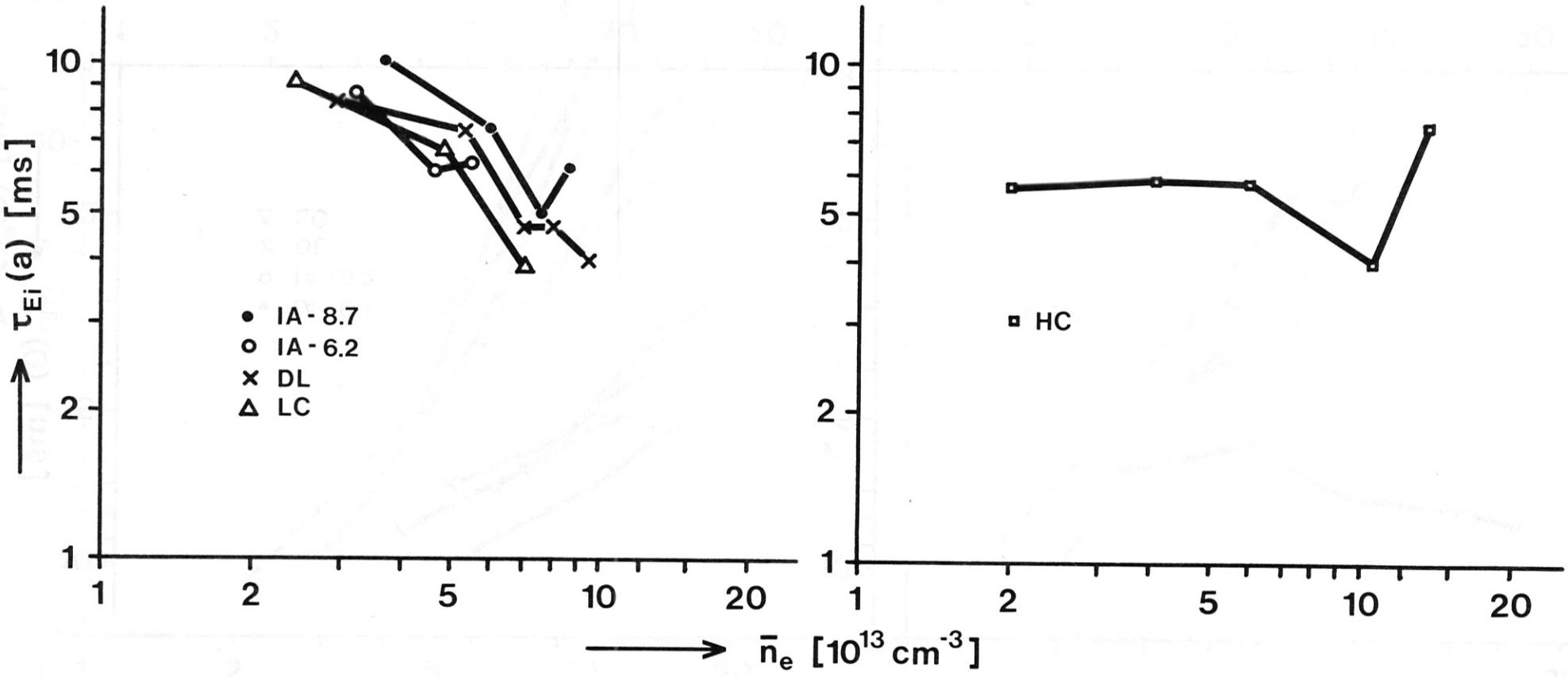

Fig. 34

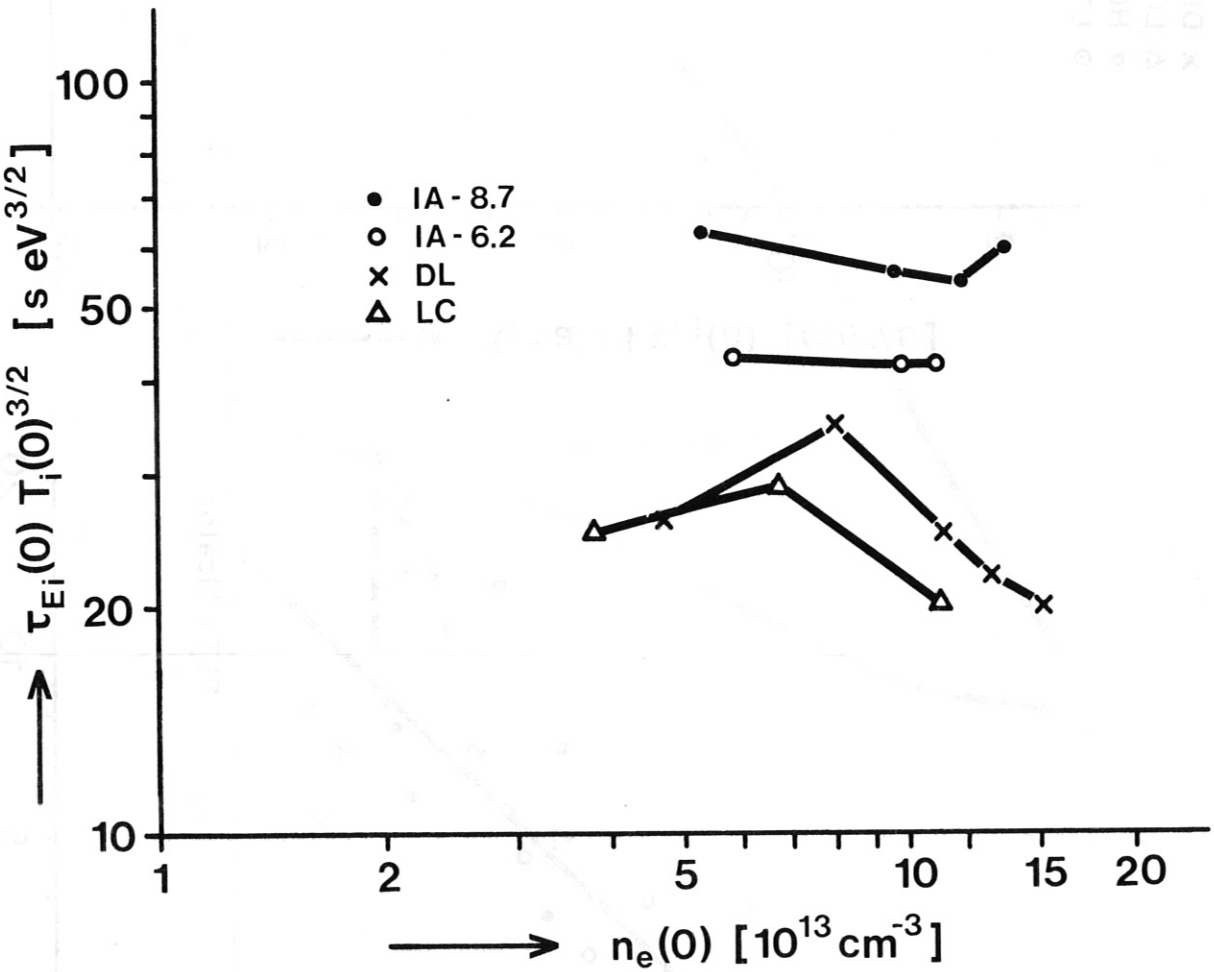
100
50
20
10
1
2
5
10
15
20
IA - 8.7
IA - 6.2
DL
LC
$\tau_{Ei}(0)\ T_i(0)^{3/2}$ [s eV$^{3/2}$]
$n_e(0)$ [10^{13} cm^{-3}]

Fig. 35

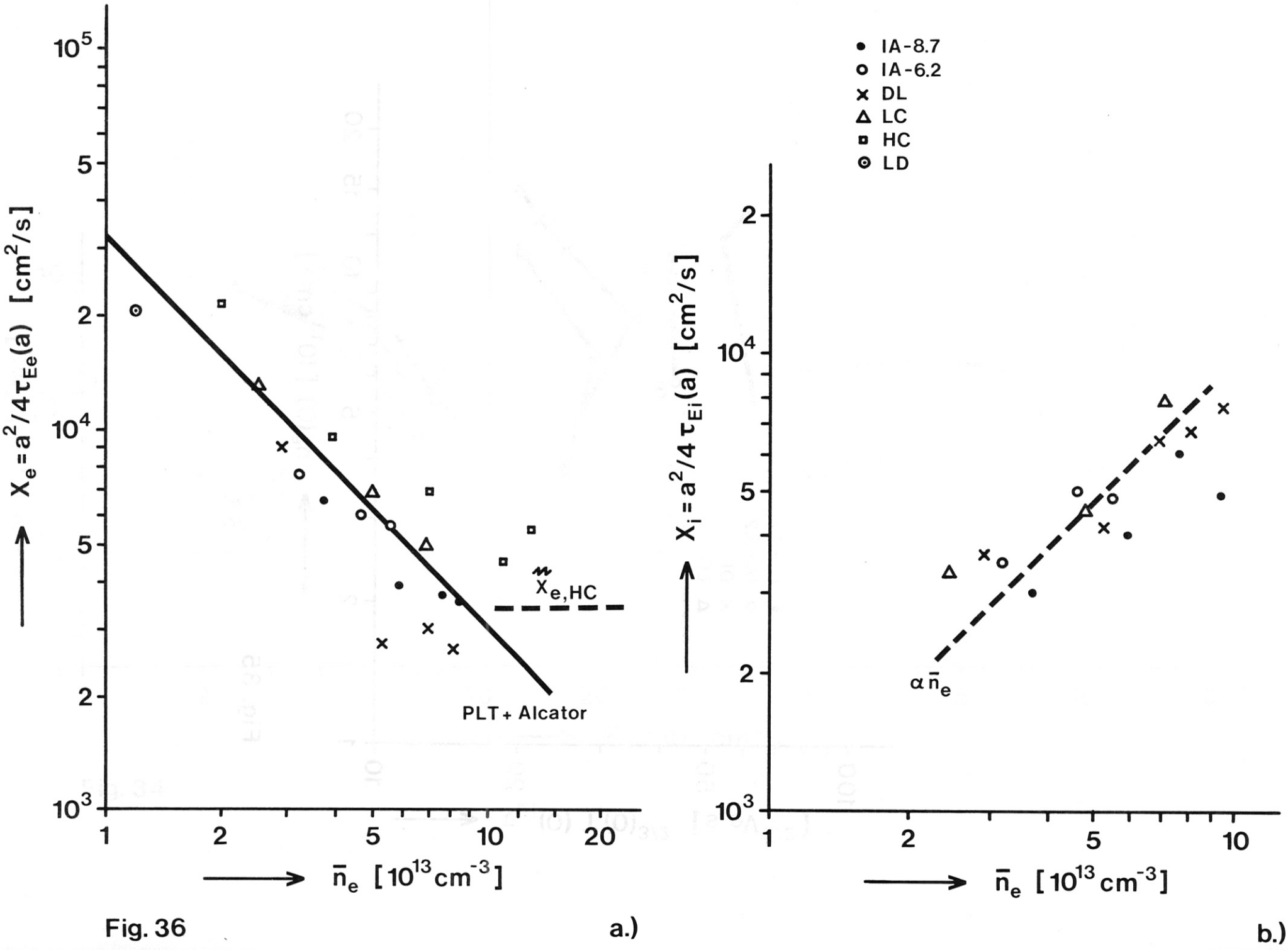
10^5
5
2
10^4
5
2
10^3
$X_e = a^2/4\tau_{Ee}(a)$ [cm^2/s]
$X_{e,HC}$
PLT + Alcator
1
2
5
10
20
$\bar{n}_e$ [10^{13}cm^{-3}]
a.)
• IA-8.7
o IA-6.2
× DL
△ LC
▫ HC
⊙ LD
2
10^4
5
2
10^3
$X_i = a^2/4\tau_{Ei}(a)$ [cm^2/s]
$\alpha \bar{n}_e$
1
2
5
10
$\bar{n}_e$ [10^{13}cm^{-3}]
b.)

Fig. 36

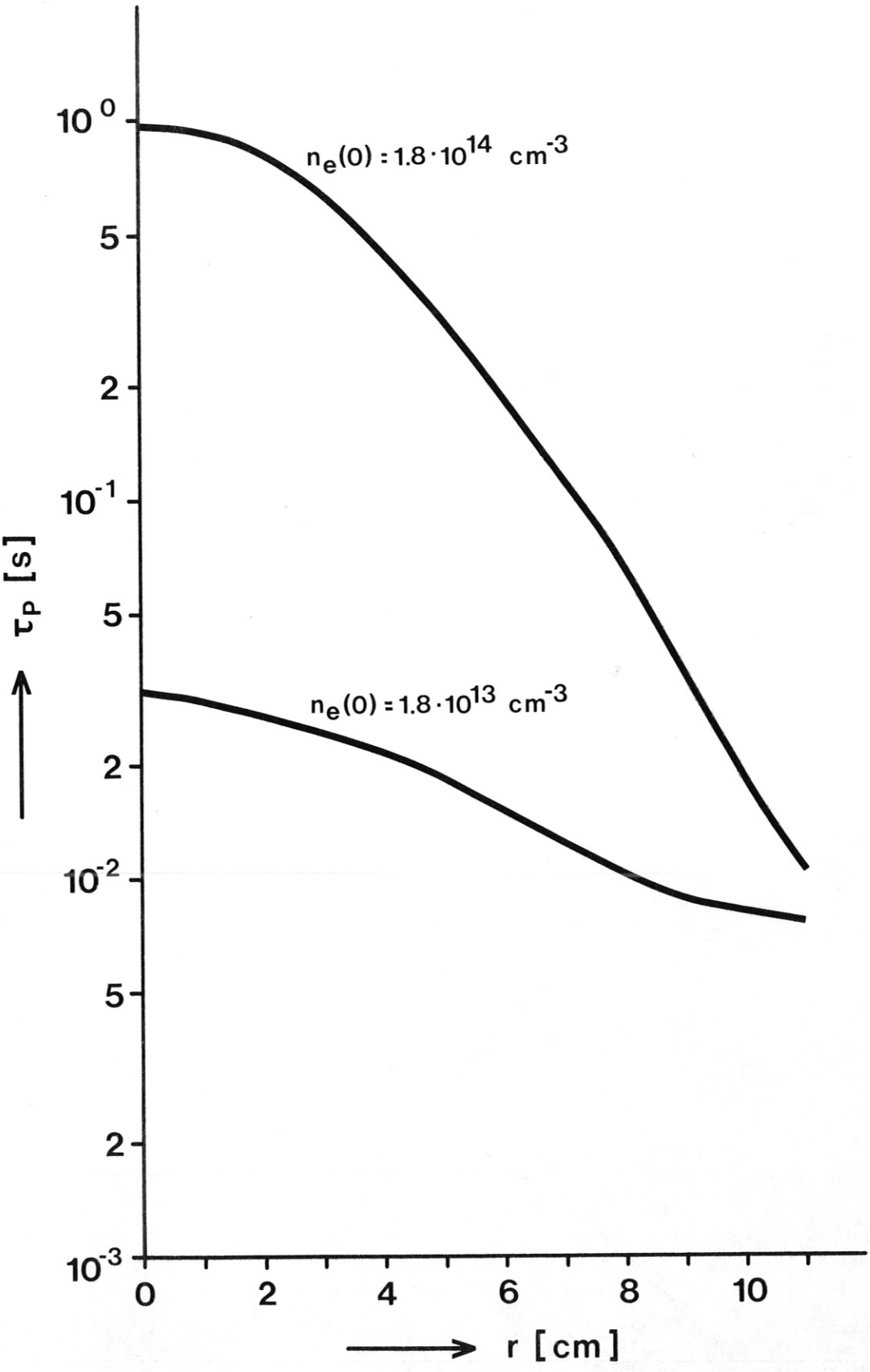
10^0
5
2
10^{-1}
5
2
10^{-2}
5
2
10^{-3}
$n_e(0) = 1.8 \cdot 10^{14}$ cm^{-3}
$n_e(0) = 1.8 \cdot 10^{13}$ cm^{-3}
τ_p [s]
0
2
4
6
8
10
r [cm]

Fig. 37